

Spitzer¹ IRS² 16 micron Observations of the GOODS Fields

Harry I. Teplitz³, Ranga Chary⁴, David Elbaz⁵, Mark Dickinson⁶, Carrie Bridge⁷, James Colbert⁸, Emeric Le Floch⁵, David T. Frayer⁹, Justin H. Howell⁷, David C. Koo¹⁰, Casey Papovich¹¹, Andrew Phillips¹⁰, Claudia Scarlata⁸, Brian Siana⁷, Hyron Spinrad¹², and Daniel Stern¹³

ABSTRACT

We present Spitzer 16 micron imaging of the Great Observatories Origins Deep Survey (GOODS) fields. We survey 150 square arcminutes in each of the two GOODS fields (North and South), to an average 3 sigma depth of 40 and 65 μ Jy respectively. We detect ~ 1300 sources in both fields combined. We validate the photometry using the 3-24 μ m spectral energy distribution of stars in the fields compared to Spitzer spectroscopic templates. Comparison with ISOCAM and AKARI observations in the same fields show reasonable agreement, though the uncertainties are large. We provide a catalog of photometry, with sources

¹Based on observations obtained with the *Spitzer Space Telescope*, which is operated by JPL, California Institute of Technology for the National Aeronautics and Space Administration

²The IRS is a collaborative venture between Cornell University and Ball Aerospace Corporation that was funded by NASA through JPL.

³Infrared Processing and Analysis Center, MS 100-22, Caltech, Pasadena, CA 91125. hit@ipac.caltech.edu

⁴MS220-6, US Planck Data Center, Caltech, Pasadena, CA 91125

⁵CEA-Saclay, DSM/DAPNIA/Service d'Astrophysique, 91191 Gif-sur-Yvette Cedex, France

⁶National Optical Astronomy Observatory, 950 North Cherry Street, Tucson, AZ 85719, USA

⁷Division of Physics, Math, and Astronomy, California Institute of Technology, Pasadena, CA 91125

⁸Spitzer Science Center, MS 220-6, Caltech, Pasadena, CA 91125

⁹NRAO, PO Box 2, Green Bank, WV 24944

¹⁰Department of Astronomy and Astrophysics, University of California Observatories/ Lick Observatory, University of California, Santa Cruz, CA 95064.

¹¹Department of Physics and Astronomy, Texas A&M University, College Station, TX 77843-4242

¹²Department of Astronomy, University of California at Berkeley, Mail Code 3411, Berkeley, CA 94720.

¹³Jet Propulsion Laboratory, California Institute of Technology, Pasadena, CA 91109

cross correlated with available Spitzer, Chandra, and HST data. Galaxy number counts show good agreement with previous results from ISOCAM and AKARI, with improved uncertainties. We examine the 16 to 24 μm flux ratio and find that for most sources it lies within the expected locus for starbursts and infrared luminous galaxies. A color cut of $S_{16}/S_{24} > 1.4$ selects mostly sources which lie at $1.1 < z < 1.6$, where the 24 μm passband contains both the redshifted 9.7 μm silicate absorption and the minimum between PAH emission peaks. We measure the integrated galaxy light of 16 μm sources, and find a lower limit on the galaxy contribution to the extragalactic background light at this wavelength to be $2.2 \pm 0.2 \text{ nW m}^{-2} \text{ sr}^{-1}$.

Subject headings: cosmology: observations — galaxies: evolution — galaxies: high-redshift — infrared: galaxies

1. Introduction

UV light absorbed by dust is primarily reradiated in the far-IR (FIR), with a peak between 60 and 100 μm . In addition, complex molecules, the polycyclic aromatic hydrocarbons (PAHs), radiate characteristic emission features in the mid-IR (MIR), the most prominent of which are at wavelengths 6.2, 7.7, 8.6, 11.3 and 12.7 μm (see Puget & Leger 1989, for a review). Over the same wavelength range, there is continuum emission from very small dust grains, which can dominate PAH emission at wavelengths beyond 10 μm (Laurent et al. 2000). The MIR flux, which results from the sum of these two emission mechanisms, correlates strongly with the integrated IR luminosity from 8-1000 μm , L_{IR} , which is a direct tracer of star formation (Kennicutt 1998; Chary & Elbaz 2001, and references therein). Active galactic nuclei (AGN) are also strong MIR sources, making the infrared an excellent tracer of obscured AGN which may not be accessible even to ultra-deep X-ray observations (Lacy et al. 2004; Sajina et al. 2005; Stern et al. 2005; Daddi et al. 2007; Donley et al. 2008). Observations from the *Infrared Space Observatory* (ISO; Kessler et al. 1996), the *Spitzer Space Telescope* (Werner et al. 2004), and the AKARI satellite (Murakami et al. 2007) have revolutionized the study of infrared luminous sources in the past decade.

Of particular interest is the measurement of the integrated galaxy light and its value compared to the DIRBE measured extragalactic background light (EBL; for a review, see Lagache et al. 2005). Lower limits on the EBL are inferred from the detection of galaxies in imaging surveys with, e.g. ISO and Spitzer (Elbaz et al. 2002; Dole et al. 2006). Upper limits on the background are obtained from γ -ray observations of blazars, because of the absorption of TeV photons by the cosmic infrared background through pair production (e.g.

Aharonian et al. 2002). More recently, Matsuura et al. (2010) have used long-wavelength (65–160 μm) AKARI imaging to directly detect the cosmic infrared background, and confirm a value in excess of the lower limit measured by stacking of Spitzer sources. Considerable effort has gone into predicting the contribution of AGN to the EBL (Fadda et al. 2002; Barmby et al. 2006; Treister et al. 2006; Ballantyne & Papovich 2007, among others). It is clear that galaxies hosting AGN do not dominate (well under 30%), but their precise contribution remains hard to estimate, in part due to the trouble identifying obscured sources. Measurement of the resolved portion of the background at a particular wavelength is performed by integrating the total flux from individually detected galaxies and through the technique of stacking.

Deep, MIR observations of the Great Observatories Origins Deep Survey (GOODS; Giavalisco et al. 2004; Dickinson et al. 2003) fields have led to important advances in understanding the global history of star formation and AGN evolution. For example, the peaks in the differential source counts at 15 and 24 microns at 0.4 and 0.2 mJy, respectively (Elbaz et al. 2002; Chary et al. 2004; Papovich et al. 2004; Marleau et al. 2004), reflect the contribution of luminous infrared galaxies (LIRGs) at higher redshifts (e.g. Pearson 2005) as MIR features redshift into the bands. The GOODS fields also provide substantial information on the presence of AGN, both obscured and unobscured, using the ultradeep Chandra observations (Brandt et al. 2001; Giacconi et al. 2002).

In this paper, we present Spitzer 16 μm observations covering the GOODS fields. We provide the source catalog, including quality assessment flags, and provide source associations between these observations and other available photometry from Spitzer, HST, and Chandra. We discuss preliminary analysis of the dataset including number counts, 16/24 μm colors, and the integrated galaxy light of 16 μm selected sources (including obscured AGN). Earlier Spitzer imaging of a small region within GOODS-North was presented in Teplitz et al. (2005).

Le Borgne et al. (2009) used an earlier reduction of the present Spitzer survey as part of a study of the cosmic star-formation history using MIR number counts. They combine a non-parametric inversion of galaxy counts at 15–850 μm with constraints from measurements of the cosmic infrared background. They exclude a major contribution from “hyper-LIRGs” at high redshift, concluding that these sources may in fact be AGN-dominated. In addition, Burgarella et al. (2009) recently reported imaging of a portion of GOODS South at 15 μm using the Infrared Camera (IRC) onboard AKARI. Their analysis has some overlap with the Spitzer study (number counts, MIR colors), and the results are consistent, as we discuss below. While the two surveys are complementary, the Spitzer study had the advantage of significantly more telescope time; it covers more area and to greater depth, especially with

the addition GOODS-North. We report ~ 1300 objects over the two fields, compared to < 300 in the AKARI survey.

We describe the survey, source extraction, quality assessment, and validation in Section 2. We provide the catalog and discuss the survey properties in Section 3. In Section 4 we describe preliminary analysis of the data, before summarizing in Section 5. Throughout, we assume a Λ -dominated flat universe, with $H_0 = 71 \text{ km s}^{-1} \text{ Mpc}^{-1}$, $\Omega_\Lambda = 0.73$, and $\Omega_m = 0.27$.

2. Observations and Data Reduction

In this section we describe the observations and data reduction. In addition, we have performed several validation checks and quality assessment measurements, which we describe in detail.

The *Spitzer* peak-up imaging (PUI) capability offered a sensitive imaging capability at $16 \mu\text{m}$ using the Infrared Spectrometer (IRS; Houck et al. 2004). The peak-up array was read out on the same detector as the Short-Low ($5\text{--}14.5 \mu\text{m}$) spectroscopic channel, in a small field of view ($56'' \times 80''$). The Si:As detector was similar to that used in the $24 \mu\text{m}$ channel of the MIPS instrument (Rieke et al. 2004). In 10 minutes of observation, the PUI achieved 5σ depths of $\sim 45 \mu\text{Jy}$.

Data were taken in two general observer *Spitzer* programs: GO-3661, observing GOODS-South in Cycle 1; and GO-20599, observing GOODS-North in Cycle 2. The southern survey was taken before the PUI mode was fully commissioned for *Spitzer*. In order to observe GOODS-South at $16 \mu\text{m}$, the instrument was commanded to take a series of short spectroscopic observations over a range of positions, and the images were acquired in parallel. Similar observations were taken over a small area within GOODS-North and are described in Teplitz et al. (2005). The northern survey used the standard PUI mode.

The southern survey was designed to consist of ~ 130 square arcminutes of shallow data (2 minutes per pointing) and 10 square arcminutes of deeper data (16 minutes per pointing) in the area of the *Hubble* Ultradeep Field (UDF; Beckwith et al. 2006). Observations were first taken in early 2005, but were compromised by persistent charge on the detector resulting from the preceding program, which targeted the rings of Jupiter. Much of the survey was repeated later in the year. Many exposures within the compromised observations were unaffected, so the shallow survey has an average of 4 minutes per pointing, with small areas of overlapping frames having greater depth. The UDF coverage varies from 16 to 32 minutes.

The northern survey covered 150 square arcminutes with ~ 10 minutes per pointing, observed in 2006. We chose not to combine these data with the previous GOODS North imaging (Teplitz et al. 2005), given the small area of the latter and the different observing modes.

IRS 16 μm images were reduced by version S13.2 of the standard Spitzer Science Center (SSC) pipeline¹. The pipeline supplied Basic Calibrated Data (BCD) frames with most instrumental effects corrected and flux calibration applied. Flux calibration was updated to match the latest version of the pipeline (S18.7). The pipeline removed a nominal low-background sky image, but some residual zodiacal light could have remained. We created median sky images from near-in-time subsets of the data, specifically from each contiguous block of observations or “astronomical observing request” (AOR). We then subtracted the median sky frames after scaling to the mode of the images.

Individual PUI frames are quite small ($56''$ by $80''$), as the primary purpose of the 16 μm camera was target acquisition. The plate scale is ~ 1.8 arcseconds per pixel. Geometric distortion is about 2%.

We registered and combined images using the MOPEX software distributed by the SSC (Makovoz & Marleau 2005; Makovoz et al. 2006a,b). We employed *drizzle* interpolation (Fruchter & Hook 2002). MOPEX *drizzle* produces the same results as *wdrizzle* in IRAF². The package uses the World Coordinate System (WCS) definition of both spatial offsets and geometric distortion. In imaging mode, the IRS did not perform an initial peak-up to refine the pointing, so the absolute WCS is good to only about 1 arcsecond, though the pointing is considerably better between BCDs within a single AOR. The Point Spread Function (PSF) at 16 μm has a full width at half maximum (FWHM) of about 3.6 arcseconds. The final mosaics have a plate scale of $0.9''/\text{pixel}$, and the *pixfrac* was set to 0.6. Figure 1 shows the mosaics of the GOODS fields.

Photometry was performed by applying a custom point source extraction code which utilizes PSF-fitting and positional priors (Chary et al. 2004). We used 5σ sources from the full GOODS IRAC channel 1 catalog (3.6 μm ; Dickinson et al. in preparation) as input. Sources within a $20'' \times 20''$ box around each input source were simultaneously fit to the measured PSF. The same technique was used in the preparation of the GOODS 24 μm catalog (Chary et al., in preparation). The PSF for each field (North and South) was measured by registering about 15 bright point sources in each field. Source position was allowed to vary by

¹<http://ssc.spitzer.caltech.edu/irs/dh/>

²IRAF is distributed by NOAO, which is operated by AURA Inc., under contract to the NSF

up to an arcsecond to account for the uncertainty in the WCS. In addition to pointing issues, this flexibility has other advantages as well, including the possibility of actual displacements between the centroids of the starlight (IRAC) and the dust emission (MIPS or IRS), or cases where IRAC sources are blended (leading to a displacement of the centroid), but where one source may dominate the MIPS or IRS emission. We checked the residual map to ensure that no sources were missed by using the IRAC priors.

The flux uncertainty was measured from residual pixels after subtracting the best-fit estimate of the source; the variance was taken as the PSF weighted sum of squares of the residuals. However, the noise in the drizzled images is correlated due to the sub-sampling. To correct for this effect, we scaled the measured uncertainty upwards by a factor of ~ 1.7 (see Casertano et al. 2000).

Photometric measurements are reported in Tables 1 and 3. We report the position of each object as that of the IRAC positional prior which was used as input to the source extraction. We cross correlated these positions with those of objects in the IRAC and MIPS 24 μm catalogs (Dickinson in prep. and Chary in prep., respectively) and report their photometry as well. The IRAC photometry was measured with SExtractor (Bertin & Arnouts 1996), using aperture photometry except in the case of a small number of extended sources for which MAG_AUTO is used.

In general, we discarded sources with less than 5σ significance. This uniform cut allows us to consider the entire survey area, despite its non-uniform coverage. Final fluxes were consistent with aperture photometry, with appropriate aperture corrections. As described below, a small number of additional sources are reported in the catalog with less than 5σ significance (with a corresponding quality flag), because they were expected to meet that criterion based upon the integration time.

Furthermore, to ensure a low incidence of spurious sources, we only used areas of the survey with good coverage. In the North and the UDF, we required at least ten individual data collection events (DCEs) per pixel. In the shallow Southern survey, this depth was not possible, but we did reject areas with less than 2 DCEs coverage. Depth of coverage is reported in the table.

The IRAC observations of the GOODS fields are much deeper than the current survey. The 3.6 μm catalog was used as input positional priors, but we can use the 8 μm data as a quality check. Even accounting for the steep slope of IR luminous galaxies, it is unlikely that real sources will be detected at 16 μm and not at 8 μm . We would reject as spurious any source which is not reported at 5σ significance in the IRAC channel four catalog. However, all sources which meet our other selection criteria pass this test. Further quality assessment

is discussed below.

2.1. Quality Assessment

We performed several quality assessment procedures in order to flag objects which may be less reliable. Flags are reported in the table.

First, we created a residual map by scaling the PSF to the measured fluxes and subtracting it from the image mosaic. We identified a small number of bright, extended objects (9 in the North and 7 in the South) for which the PSF-fit photometry is inappropriate. We measured these sources in a large aperture instead. A flag for extended sources is reported in the table.

Second, we estimated the concentration of detected objects by measuring the ratio of aperture photometry in 6 and 2 pixel radii. Objects which are point sources should fall in the range of $\sim 2 - 3 : 1$. Objects outside the nominal range (ratio > 4 or < 1.3) are flagged in the catalog. Several objects with anomalous values were inspected by eye and rejected from the catalog.

Third, we flagged objects which may be affected by source confusion. We identified close companions in the catalog, within a radius of 5.4 arcseconds (6 pixels, a little larger than the FWHM of the PSF). We also flagged targets which have 8 μm sources (detected at $> 3\sigma$) within 4 arcseconds, whether or not they are detected at 16 μm .

Fourth, we compared the signal to noise ratio (SNR) estimate from our photometry code to the expectation from the exposure time map. The exposure time calculator at the Spitzer Science Center website predicts a 1σ sensitivity of $\sim 50 \mu\text{Jy}$ in a single 30 second exposure, and the observations are background limited so sensitivity is expected to scale with the square root of exposure time. The measured SNR generally agrees within about 20% with expectations, though our estimates are slightly conservative. A small number of objects were selected as meeting the 5 sigma cut but exceeding the expected sensitivity; that is, they would have been excluded using the expected noise values. We retain these objects and flag them as long as the expected SNR is 4 or greater. Conversely, a somewhat larger number of objects were expected to meet the 5 sigma cut but did not in our measurements. We report such objects as low confidence sources as long as they have measured SNR greater than 4.

Finally, we flagged sources with the spectral energy distribution (SED) expected for stars. Specifically, we identified stars as those objects for which the flux density is declining

across all six bands. We exclude one object for which $f_{24} > f_8/2$, which can be the case for some low redshift galaxies. Of these, 7 (2) in the N (S) are confirmed as stars in ground-based spectra. In the North, we also flag as stars two sources that are saturated in IRAC channel 1 (which causes them to fail the SED check) but are confirmed in ground-based spectra. We check all star identifications in the ACS imaging of the GOODS fields and confirm that they are point sources. The imaging also shows that two of the objects identified as stars in the North are likely confused with nearby galaxies, and we flag these separately (see Section 3).

2.2. Photometric Calibration and Verification

The calibration of the Spitzer Peak-Up Imaging mode is in the IRS Instrument Handbook³ and briefly summarized here. The current calibration is based upon spectroscopic and imaging observation of four A stars for which detailed spectral models were available. There is a systematic uncertainty of $\sim 5\%$ in the calibration.

Stellar fluxes were measured from the the IRS spectra of the calibrators by integrating under the filter transmission curve and color-correcting to the effective wavelength ($15.8\ \mu\text{m}$) assuming $\nu F_\nu = \text{const.}$ This assumption is designed to keep the color correction small for a wide range of spectral slopes. The calibration is normalized to infinite aperture using Tiny Tim V2.0⁴. In practice, aperture photometry requires an aperture correction. Profile-weighted fitting, such as that utilized in the present study, is normalized to a finite radius and then aperture corrected as well.

The PUI calibration is tied to the calibration of the spectrometer, which has been validated against a large number of stars. To evaluate the calibration in the particular case of the GOODS data, we can compare the photometry of stars within the two fields. Twenty-five objects have IRAC colors clearly indicative of stars. However, four of these objects have quality flags greater than 1, so we exclude them. We also exclude another 6 objects that have SEDs indicating possible IR excesses. So, we have 15 stars with which to validate the PUI calibration. These objects are faint, however, and we do not know their stellar types. Nonetheless, the mid-infrared spectral energy distribution of stars does not vary much across a wide range of stellar types. The Spitzer Atlas of Stellar Spectra (SASS, Ardila et al. in preparation) observed stars across many stellar types with the IRS. In Figure 2 we plot the photometry for the 15 stars compared to SASS IRS spectra of stars with types A through

³<http://ssc.spitzer.caltech.edu/irs/irsinstrumenthandbook/>

⁴<http://ssc.spitzer.caltech.edu/archanaly/contributed/stinytim/index.html>

M, excluding super giants, and the Kurucz (1979) model for an A0V star. We apply a small ($< 4\%$) color-correction to the photometry to account for the difference between the assumed calibration reference spectrum ($\nu f_\nu = \text{const}$ for IRAC⁵ and PUI; 10^4 K black body for MIPS⁶) and a typical (5000 K black body) stellar spectrum. The spread in photometry is similar to the expected variation within stellar types, and does not indicate systematic offsets in the photometric calibration.

2.3. Comparison with ISOCAM and AKARI

In addition to validation using stars, we compare *Spitzer* photometry to other observations of the field at similar wavelengths.

ISOCAM (Cesarsky et al. 1996) on-board the *Infrared Space Observatory* observed a portion of GOODS-North centered on the Hubble Deep Field North (Williams et al. 1996). Careful reduction of those data was presented by Aussel et al. (1999). The ISOCAM catalog reports 40 objects detected at $15\ \mu\text{m}$ in the main catalog. Of these, 36 are associated with sources in the *Spitzer* $16\ \mu\text{m}$ catalog. The four unmatched sources are all fainter than $100\ \mu\text{Jy}$, and two of them do not appear in the (deeper) $24\ \mu\text{m}$ catalog, indicating that they are probably spurious. Figure 3 shows the comparison of *Spitzer* and ISOCAM fluxes for matched sources.

Both ISOCAM and *Spitzer* PUI are calibrated assuming $\nu f_\nu = \text{const}$, but the effective wavelengths are substantially different, being 14.3 and $15.8\ \mu\text{m}$, respectively⁷. So, a color-correction to the ISOCAM photometry equal to the ratio of the effective wavelengths – e.g., a factor of 1.1 – is expected. We fit the offset between *Spitzer* and ISOCAM photometry assuming a constant slope of unity and find *Spitzer* fluxes to be 1.13 times brighter. Overall, we see general agreement within the large error bars. *Spitzer* had better spatial resolution at $16\ \mu\text{m}$ than ISOCAM, and some of the ISOCAM sources are blends of multiple objects, and this may explain the difference in flux for some objects. The four brightest objects do not appear to suffer from blending, however.

As noted in Teplitz et al. (2005), the difference in filter bandpasses can cause substantial differences in the reported flux densities at some redshifts (up to a factor of 1.5 or even 2) as prominent MIR features move in and out of the filters. Figure 4 shows the ratio of *Spitzer*

⁵IRAC Instrument Handbook; <http://ssc.spitzer.caltech.edu/irac/iracinstrumenthandbook/>

⁶MIPS Instrument Handbook; <http://ssc.spitzer.caltech.edu/mips/mipsinstrumenthandbook/>

⁷See the “ISOCAM Photometry Report”, 1998; http://www.iso.vilspa.esa.es/users/expl.lib/CAM/photom_rep_fn.ps.gz

to ISOCAM fluxes for objects with known redshifts (see Section 3.2).

The four brightest objects in common between Spitzer and ISOCAM show a larger offset in photometry than is typical for the sample as a whole. The differences may result, in part, from the difference in filter bandpasses as shown in Figure 4. All four objects are detected by Chandra (see Section 3.3), two of them in the hard band. The sources do not appear to be variable, however, as all four were also detected by Spitzer in independent measurements (Teplitz et al. 2005), and their flux densities agree within 10%.

Burgarella et al. (2009) used the IRC on-board the AKARI satellite to observe a $\sim 10' \times 10'$ region partially overlapping with GOODS-South. Their catalog contains 67 objects detected at $> 5\sigma$ in areas which we observed with sufficient coverage (at least 2 DCEs). Of these, 60 have associated sources within $3''$ (two IRC pixels) in the Spitzer catalog. Figure 5 shows the comparison of Spitzer and AKARI flux densities for matched sources. AKARI IRC is also calibrated assuming $\nu f_\nu = \text{const}$, but with an effective wavelength of $15.0 \mu\text{m}$, implying a color correction between the filters of 1.06. However, the best fit to the photometry shows a difference in photometry of a factor of 1.3. The filter bandpasses are slightly different, with the IRC filter being considerably wider, which may account for some of the difference.

3. Results

Extracted sources are given in Tables 1,2 and 3,4 for GOODS-N and GOODS-S, respectively. The tables include ancillary data from other telescopes, together with other Spitzer photometry in the IRAC and MIPS $24 \mu\text{m}$ channels. Quality flags are given in the tables; caution is recommended in the interpretation of results based upon sources that do not have quality 1.

Specifically, the tables provide the available data on each source: position, photometry and uncertainty from Spitzer, HST, and Chandra, spectroscopic redshifts where available, and quality flags. The process for identifying HST, Chandra and redshift associations is given later in this section. Details of the columns in the table are given below:

- Column (1) gives the source ID number within the catalog.
- Columns (2) and (3) give the right ascension and declination (J2000) of the source. Positions are reported as the IRAC prior position used as input to the source extraction.
- Column (4) gives the coverage (in number of exposures) of the central pixel of each source. Exposure times were 30 (N) and 60 (S) seconds.

- Columns (5) through (16) give the IRAC channels 1-4, IRS 16 μm , and MIPS 24 μm flux densities and uncertainties for the source, in units of μJy . Uncertainties are given after each photometric point (e.g. Column 5 is photometry, Column 6 is uncertainty). The IRAC uncertainties include a 5% systematic uncertainty in the calibration (added in quadrature to the measured uncertainty). This systematic term dominates the uncertainty for most objects, especially in channels 1 and 2.
- Column (17) gives the spectroscopic redshift for the source, where available. Spectroscopic counterparts were usually chosen to be the closest optical/NIR object to the 16 μm position. In a few cases, the 16 μm emission is likely due to a blend of sources, and the slightly more distant one is the more likely dominant counterpart. A value of -99 indicates that no redshift is available. The very few stars with spectra are listed with $z=0$.
- Column (18) gives the reference code for the spectroscopic redshift (see Section 3.2). Redshifts were collated from the literature, as well as from observations by the GOODS team (Stern et al. in prep.).
- Column (19) indicates that the source has non-zero flux in at least one Chandra band (a value of 1 is detected).
- Column (20) and (21) give the soft and hard X-ray fluxes, respectively, for the associated *Chandra* detection.
- Column (22) is a star flag, with a value of 1 indicating the source is likely a star. A value of 2 indicates that the position of the IRAC prior is confused between a star and a neighboring galaxy (there are two such cases in the Northern field).
- Column (23) gives the 16 μm concentration index, defined to be the ratio of flux within apertures of radii 6 and 2 pixels.
- Column (24) gives the number of 8 μm sources within 4 arcseconds.
- Column (25) gives the number of 16 μm sources within 5.4 arcseconds.
- Column (26) gives the bit-wise quality flag for the source: Bit 0 – the object was determined to be real and included in the catalog; if only this bit is set, then there are no notes and the object has the best quality; Bit 1 – possible confusion because more than one 16 μm source lies within 5.4 arcseconds; Bit 2 – bad concentration index; Bit 3 – low SNR but the source was included because the expected SNR was at least five. In GOODS-S, we also include a flag for Bit 4, in the case of sources with coverage of

two exposures instead of three. Because flags are assigned bit-wise, sources may have multiple flags set. So, for example, an object with a flag value of 19 would indicate that Bits 0,1, and 4 had been set because: (Bit 0) the object was included in the catalog; (Bit 1) the measurement of the object may suffer from confusion due to a close $16\ \mu\text{m}$ neighbor; and (Bit 4) the object had a coverage of only two exposures.

- Column (27) flags extended sources which were measured with aperture photometry instead of the PSF-fit. A value of 1 indicates that the source was extended.
- Column (28)-(31) give the HST magnitudes for the B,V,I,z bands respectively (see Section 3.1).
- Column (32)-(35) give the HST uncertainty (in magnitudes) for the B,V,I,z bands respectively.
- Column (36) gives the number of I-band sources within 1 arcsecond radius.

We report the detection of 840 (North) and 476 (South) sources.

The depth achieved in the survey is consistent with expectations. The 5σ limit in the shallow Southern area varies from ~ 65 to $85\ \mu\text{Jy}$. The UDF limit is $\sim 30\ \mu\text{Jy}$, though the small area means that there are few objects even in the faintest bin. The Northern survey reaches $\sim 40\ \mu\text{Jy}$. Figure 6 shows the area covered in bins of predicted sensitivity. Table 5 summarizes the number of objects in each field, and in some sub-categories (see below). Table 6 lists the predicted and achieved depths for the North, South, and UDF regions.

In the remainder of this section, we examine the association between $16\ \mu\text{m}$ sources and other measurements within the GOODS fields.

3.1. Optical Photometry

We use the optical photometry from the publicly released GOODS version 2.0 catalogs (Giavalisco et al. 2004)⁸. We use the reported MAG_AUTO fluxes. We cross correlate the positions of $16\ \mu\text{m}$ detections with those of optical sources within 1 arcsecond. The GOODS catalogs used the z -band images for source detection and then measured photometry in the other three optical bands.

⁸<http://archive.stsci.edu/prepds/goods/>

Of the 840 sources in the north, 809 have associated optical sources within 1 arcsecond. In the South, 465 of 476 sources in the 16 μm catalog have optical associations. Of the 31 (N) and 11 (S) sources without an associated optical detection, 11 (N) and 4 (S) do not have coverage in the ACS mosaics. For objects with coverage, 6 (N) and 4 (S) are near the diffraction spikes from bright stars, and 6 (N) and 1 (S) are in the outskirts of extended galaxies. The remaining 8 (N) and 2 (S) sources may be very red, or they may have a larger uncertainty on the centroid – either due to Spitzer pointing uncertainty or to blending with another source in the IRAC positional priors. For matched sources, the possibility of source confusion is significant when matching MIR and optical sources. We find 57 (N) and 37 (S) sources have multiple possible optical matches within 1 arcsecond, and we report the closest one to the IRAC position. The number of close matches is flagged in the table.

3.2. Redshift Distribution

Spectroscopic redshifts have been measured for sources in the GOODS fields by numerous surveys. The specific spectroscopic surveys used are given in the tables.

We correlate the positions of detected Spitzer sources with redshift identifications within about 1 arcsecond radii. In cases for which multiple optical sources are within 1 arcsecond of the 16 μm target, we usually take the closest positional match. In a few cases the 16 μm emission is likely due to a blend of sources, and the slightly more distant one is the more likely dominant counterpart. Another 21 (N) and 8 (S) objects have optical sources in the redshift catalogs between 1 and 2 arcseconds away, allowing the possibility for misidentification in those cases as well. Redshifts are reported in the table. In the North 701 redshifts are available out of 826 objects not identified as, or confused with, stars. Most (654) of the redshifts are for objects with $i_{AB} < 24$, and at that magnitude, redshifts are available for 94% of 16 μm sources. In the South, 381 redshifts are available out of 466 galaxies detected. Only 36 of the spectroscopic redshifts in the South are for objects fainter than $i_{AB} = 24$, and 87% of 16 μm targets down to that magnitude have redshifts. For comparison, there are 828 redshifts associated with 5σ 24 μm detections in the North and 814 in the South.

Figure 7 shows the redshift distribution of detected 16 μm sources. It appears that the distribution of associated redshifts is similar for 24 and 16 μm sources at redshifts less than 1.5. At higher redshifts, there are significantly more 24 μm detections, as a result of both the greater sensitivity of the MIPS observations and the intrinsic brightening of starburst sources when the strong PAH features shift into the 24 μm band. The similarity of the distributions at lower redshifts suggests that the distribution may be a stronger function of the optical limits on obtaining redshifts rather than the MIR observations themselves. Figure 8 shows

the 16 μm flux density versus redshift.

The median spectroscopic redshift, excluding stars, for 16 μm sources is 0.85 (N) and 0.82 (S), and the mean is 0.86 in each field. About 30% of redshifts in the North are at $z > 1$, and about 35% in the South. About 2% of the sources in each field (13 North, 6 South) have $z_{\text{spec}} > 2.0$. Most of these (\sim half in the North and 5/6 in the South) are identified as AGN, as described below. The highest spectroscopic redshifts for 16 μm sources are 3.48 (N) and 3.47 (S).

3.3. X-ray Sources

The *Chandra* 2 Msec surveys of the GOODS North and South fields, respectively, are the deepest X-ray observations taken to date. We compare the 16 μm survey to the *Chandra* catalogs of Alexander et al. (2003) and Luo et al. (2008). There are 308 (N) and 293 (S) X-ray sources within the GOODS area surveyed at 16 μm . Of these, 117 (N) and 92 (S) are associated with 16 μm sources, comprising 14% and 20% of the 16 μm samples. Sources that are detected in the *Chandra* catalogs are flagged in the table.

4. Discussion

4.1. Active Galactic Nuclei

The detection of sources at 16 μm selects both strongly star-forming galaxies and those which host AGN. Most sources in the present survey lie at redshifts below 2, which ensures that the PUI passband samples the wavelength range that covers emission by dust rather than direct stellar light. At $z > 1$, the PUI band is increasingly dominated by hot dust characteristic of AGN, and at $z > 2$ the sensitivity of the survey is mostly limited to such sources.

Hard X-rays are usually indicative of an AGN. The ultradeep *Chandra* data select many of the AGN within GOODS. There are 96 (N) and 58 (S) PUI sources associated with detections in the hard band. Given the depth of the CDFs, a few of these objects may have X-rays from purely star-forming galaxies. For example, Treister et al. (2006) excluded sources with $L_X < 10^{42}$ ergs s^{-1} when selecting AGN in GOODS. The fraction of such sources is small amongst 16 μm targets, and the exact nature of those sources is uncertain, so we retain them as possible AGN in this analysis.

Some galaxies hosting AGN, even those whose bolometric luminosity is dominated by

them, are undetected even by *Chandra*. These sources may be selectable using their MIR color, when AGN heated dust dominates over stellar light. In many cases, these will have power-law SEDs (e.g. Donley et al. 2007). We perform a χ^2 fit to the IRAC+16 μm colors to identify power-law sources. We fit all SEDs with a power-law, $\nu^{-\alpha}$, and select those with $\alpha > 0.25$. We do not set a limit on the goodness-of-fit, but we exclude sources where the channel 3 or 4 flux does not exceed the channel 1 flux. Using only IRAC photometry with 16 μm does not significantly change the results. We find about 10% more AGN when combining X-ray with power-law selection than when using x-ray selection alone. Conversely, we find that about 45% of hard X-ray sources have power-law SEDs.

A similar fraction was measured by Barmby et al. (2006), who found that $\sim 40\%$ of X-ray sources in the extended Groth Strip have red power-law SEDs in the IRAC bands.

Combining the two selections, we find 105 (N) and 65 (S) AGN. These numbers are likely to be a slight underestimate, as they may not include Type 2 AGN whose IRAC colors are not true power-laws. Nonetheless, we find that about 15% of 16 μm sources are galaxies hosting AGN. Figure 9 shows the fraction of sources with AGN in bins of 16 μm flux density. The fraction is higher for the brighter sources.

Amongst rare, bright sources, obscured AGN may be more common. Stern et al. (2005) identify QSOs and Seyfert 1 galaxies as objects with red IRAC colors, but their selection is contaminated by star forming galaxies at the faint fluxes, such as those in the GOODS survey. Donley et al. (2007) find that when using the IRAC color-color selection only 55% of MIR power-law AGN are detected in the X-ray.

Treister et al. (2006) find a decreasing AGN fraction with decreasing 24 μm flux for sources in the GOODS fields, down to $\sim 8\%$ at $< 100 \mu\text{Jy}$ using purely hard X-ray selection. The fraction of X-ray sources at 16 μm is similar, as expected given the high rate of detection of *Chandra* sources. Donley et al. (2008) also find a decreasing AGN fraction with decreasing 24 μm flux, down to about 10% X-ray AGN. They then expand the estimate to MIR-selected AGN and estimate about 15–25% at 100–300 μJy , similar to our estimate given the large error bars.

Table 5 summarizes the numbers of AGN per field.

4.2. 16 to 24 μm Color

One of the most prominent MIR spectral features is the broad (full width $\sim 2 \mu\text{m}$) silicate absorption trough at 9.7 μm . Attenuation at this wavelength can approach an

order of magnitude in typical ultraluminous IR galaxies (e.g. Armus et al. 2004). As a result, this feature will significantly depress the photometry measured in a broad-band filter. Takagi & Pearson (2005) suggested that the 16 to 24 μm ratio can be used to identify “silicate-break” galaxies, at redshifts $1.1 < z < 1.6$ where the silicate absorption is solidly within the MIPS 24 μm bandpass.

Figure 10 shows the S_{16}/S_{24} ratio of catalog sources for which spectroscopic redshifts are available, and which are solidly detected in the 24 μm band. We apply a small color correction (4%) to the MIPS 24 μm flux densities in order to account for the difference in the way the instruments are calibrated. The PUI is calibrated assuming a reference spectrum of $\nu F_\nu = \text{const}$, but MIPS is calibrated using a 10^4 K black body (see the MIPS Instrument Handbook).

Much of the scatter in the flux ratio is expected due to variation in the source SEDs. We demonstrate this by calculating the expected ratio for redshifted local template sources. Smith et al. (2007) obtained Spitzer IRS spectra for a range of local starbursts, and found a large variation in both PAH emission strength and silicate absorption depth. They find that the relative strength of features can vary by a factor of two in star forming galaxies ($L_{\text{IR}} < 3 \times 10^{11} L_\odot$) depending upon source properties, though they note the variation should be somewhat less in more luminous sources. Brandl et al. (2006) also measured local starbursts, notably NGC 7714, and calculated an average starburst spectrum, which is redder than the Smith et al. templates, and so results in a lower expected ratio. In the plot, we indicate the expected ratio for these templates as a shaded region. Similar results have already been reported by Burgarella et al. (2009) using the AKARI measurements in GOODS-S. They find that local starburst templates mostly reproduce the flux ratio well, but that there are some discrepancies at higher luminosities. The AKARI survey was limited to $z < 1.2$.

Armus et al. (2007) calculated the expected 16 to 24 μm ratio for local ultraluminous IR galaxies (ULIRGs), and found that it is significantly lower than for starbursts at most redshifts because ULIRGs have a red continuum. However, in the redshift range for which the silicate absorption falls in the 24 μm passband, the ratio can be extreme (> 3 for some ULIRGs). In the Figure we plot the ratio using Arp 220 as a representative ULIRG template. Finally, we note that AGN lacking strong silicate or PAH features will have red colors at all redshifts. Figure 10 also shows the ratio for an AGN with a very red ($\alpha = -2$) power law SED ($f_\nu \propto \nu^\alpha$).

For clarity, error bars are omitted from points in the figure within the expected region. Typical uncertainties are 0.1-0.2 in the flux ratio. Instead, we only plot individual uncertainties for objects with 16/24 colors more than 1σ bluer than the expected regions. There

is significant scatter in the plot, but a trend at $z > 1$ indicating the presence of silicate absorption is present.

A number of sources at $z < 1.1$ are anomalously blue, though most of them are likely the result of measurement error (large uncertainties) or data quality issues (most have quality flag warnings, as shown in the figure). The rest may have SEDs that are bluer than local starbursts because the 24 μm band is tracing longward of 12 μm emission and their warm dust contribution is low.

Objects at $1.1 < z < 1.6$ with a ratio bluer than $S_{16}/S_{24} = 1.2$ lie solidly in the region expected for silicate absorption. Kasliwal et al. (2005) used the same selection when identifying silicate absorbing sources in early Spitzer observations of the NOAO Deep Wide Survey field. However, many objects at lower redshifts fall within the same cut. Selecting objects with a ratio > 1.4 eliminates many, though not all, of the low redshift interlopers. If we consider only sources with a 16 μm quality flag of 1 and an available spectroscopic redshift, then 10 of 44 selected sources are outside the redshift range for silicate absorption. For comparison, $\sim 80\%$ of 16 μm sources with spectroscopic redshifts are at $z < 1.1$. If we consider all sources which are securely detected at 24 μm and have available redshifts (regardless of quality flag), then 33 of 91 sources are possible interlopers; however, about half of these have quality flag with either Bit 1 or Bit 2 set, indicating possible confusion or a bad concentration index. We note that not all objects with blue ratios are true silicate absorbers. Many, perhaps most, are star-forming galaxies where the blue color results from the dip between the 7.7/8.6 and 11.2/12.7 μm PAH complexes (Smith et al. 2007).

A few objects lie at redshifts higher than the range where silicate absorption falls in the 24 μm band but still have colors bluer than expected for either AGN or the starburst template. These objects could have buried AGN causing large hot dust emission at 5-6 μm , or they could have anomalously strong 6.2 PAH features.

Figure 11 shows the flux ratio for objects selected as AGN by either power-law SEDs or hard X-ray detection. The $S_{16}/S_{24} > 1.4$ selection does not appear to select objects that are dominated by known AGN. In the Figure, we also see a number of AGN sources with very low S_{16}/S_{24} ratios. At $z \sim 0.6$, some of these may be explained by silicate absorption in the 16 μm band. Of course, the ratio will be low for objects with red SED as well, so the silicate selection is not as clean.

Figure 12 shows histograms of the flux ratio for the 16 μm sample, and the AGN subset. Applying the ratio cut at 1.4 (and excluding sources with other spectroscopic redshifts), we find 107 blue sources, of which possible 68 have a quality flag of 1, which could indicate that they are $z \sim 1.3$ sources. Table 5 compares these numbers with the AGN selected for each

field.

4.3. Number Counts

We calculate galaxy number counts for each field. First, we determine the area, A_i , over which each source could have been detected assuming our estimate of the sensitivity based upon the depth of coverage. Then, we sum the reciprocal of the area for each source within logarithmically spaced bins of flux and divide by the binwidth, δ_f .

$$nc = \frac{1}{(\delta f)_{bin}} \sum_{i_{bin}} \frac{1}{A_i} \quad (1)$$

This calculation does not include the effects of source confusion which could lead to slightly under-counting the number of galaxies. We estimate the uncertainty on the counts for each bin as the Poisson error in the measurement of the number of sources in the bin.

Completeness corrections were calculated using a Monte-Carlo simulation, following Chary et al. (2004). Separate simulations were performed for the three depth tiers of the survey – GOODS-North, GOODS-South, and the UDF. Artificial sources were added to the original data images and recovered. These sources were placed at random positions. The flux distribution of simulated sources was flat in $\log(f_\nu)$. The fluxes varied from 20 to 1000 μJy . To avoid confusion of simulated sources, only a small number were added at a time and the simulation was repeated many times. In the North and South, 50 objects were added to the images at a time, with the simulation repeated to build up ten thousand simulated input sources. In the UDF, only 15 sources were added at a time. Sources were recovered using the same positional prior code used for the catalog generation, discarding sources below 5σ . The completeness of recovered sources is seen to be worst at the faint fluxes, as expected. There is considerable incompleteness at relatively bright fluxes, as well, due to confusion of simulated and real sources. This effect appears to be on the order of 5–10%.

A matrix P_{ij} for the output flux distribution of the artificial sources was generated, where i is the input flux and j is the recovered flux (Smail et al. 1995). The classical completeness for sources in the i^{th} bin is the ratio of number of recovered sources in that bin to the sum over all j for that bin. The observed catalog of sources in the real image was then distributed among the flux bins. The P_{ij} matrix was renormalized such that the sum over i for each j was equal to the number of detected sources in that flux bin. The completeness corrected counts in each flux bin i is then the sum over j of the renormalized P_{ij} matrix.

In the North, we estimate completeness to be $\sim 50\%$ at 40 μJy (the approximate limit

of reported sources), and 80% at 60 μJy . In the South, we estimate 80% completeness at 80 μJy in the shallow survey, with a steep fall off at fainter fluxes due to poor coverage. In the calculation of the number counts, we do not use the shallow Southern survey below 65 μJy . In the UDF, we estimate 50% completeness at 30 μJy (the limit of reported sources) and 80% at 50 μJy .

Figure 13 shows the measured number counts, including the completeness correction described below. The figure also compares 15 μm number counts from ISOCAM and AKARI, but without color-correction. Le Borgne et al. (2009) showed that these number counts are dominated by low redshift objects ($z < 0.5$) at fluxes above 200 μJy , and by moderate redshift ones ($0.5 < z < 1.5$) at fainter levels; they infer a small contribution ($< 20\%$) from higher redshift sources in bins below 100 μJy .

In the figure, we see a significant difference between the counts in the Northern and Southern fields. The counts peak around 0.4 mJy in the North, but around 0.2 mJy in the South. It is likely that this effect is the result of cosmic variance. However, the distribution of redshifts (see Section 3.2) shows no clear evidence for an over-density in the Northern field to explain the difference. LeFloc’h et al. (2009) noted a similar effect in comparing GOODS-North counts at 24 μm to those in the (wider area) COSMOS field.

Elbaz et al. (1999) measured a faint-end slope of $\alpha = -1.6$ from the ISOCAM 15 μm counts. They defined the faint-end to be bins with $S_{15} < 0.4$ mJy. In the same range, we measure a slightly steeper slope of -1.9 when fitting the counts from both the North and South. However, the fit is dominated by the high significance bins between 0.1 and 0.4 mJy, where the two fields have different peaks. If we consider only $S_{16} < 0.2$ mJy, then $\alpha = -1.7$ is consistent with the data.

In Figure 14, we show the contribution of AGN to the number counts. The result is largely similar to Figure 9, with X-ray selected AGN dominating the AGN contribution at bright fluxes, and the total AGN contribution decreasing at faint fluxes. We also show in the figure the contribution of silicate absorption candidate sources, which could be highly obscured AGN. These objects occur mostly at faint flux levels, given their high redshift.

4.4. Integrated Galaxy Light at 16 microns

Previous measurements of the monochromatic 15 μm EBL have been based on ISOCAM and AKARI data (Elbaz et al. 2002; Altieri et al. 1999). Metcalfe et al. (2003) inferred the contribution of ISO-detected galaxies to the 15 μm EBL to be 2.7 ± 0.62 nW m^{-2} sr^{-1} at $S_{15} > 30$ μJy by integrating the flux measured from faint sources (the integrated galaxy

light, IGL) including the observations of lensing clusters. Hopwood et al. (2010) improved the measurement of the lensing cluster and determined an IGL value of $1.9 \pm 0.5 \text{ nW m}^{-2} \text{ sr}^{-1}$ at $S_{15} > 10 \text{ } \mu\text{Jy}$.

We can improve the measurement of the $\sim 15 \text{ } \mu\text{m}$ IGL using the Spitzer sources. We have significantly more detections fainter than $50 \text{ } \mu\text{Jy}$ than any of the ISOCAM surveys, and we cover two independent fields that were covered by the ultra-deep AKARI measurement. We first take the average of the number counts for both GOODS fields, and combine them with ISOCAM counts at fluxes $> 1 \text{ mJy}$ (Elbaz et al. 1999; Gruppioni et al. 2002). Next, following Elbaz et al. (2002), we integrate $dIGL/dS$ (defined by their Equation 6) over the range $30 \text{ } \mu\text{Jy}$ to 1 mJy , after fitting the counts with a 3^{rd} degree polynomial (the dotted line in Figure 13). A conservative estimate of the uncertainty on IGL_{15} was obtained by fitting and integrating the Poissonian upper and lower 1σ uncertainty on the counts.

We find $IGL_{16} (S_{16} \geq 30 \mu\text{Jy}) = 2.2 \pm 0.2 \text{ nW m}^{-2} \text{ sr}^{-1}$. Note that if we color-correct the Spitzer sources to the effective wavelength ($14.3 \text{ } \mu\text{m}$) of the ISOCAM LW3 filter as in Figure 3, we would obtain $IGL_{15} (S_{15} \geq 25 \mu\text{Jy}) = 1.8 \pm 0.2 \text{ nW m}^{-2} \text{ sr}^{-1}$, just outside the 1σ uncertainties from the Metcalfe et al. (2003) result. Figure 15 shows the IGL as a function of sensitivity limit. The upper limit on the EBL, $4.7 \text{ nW m}^{-2} \text{ sr}^{-1}$ is taken from the Renault et al. (2001) high energy γ -ray measurement of Mrk 501. Comparing the upper limit to the EBL, following Metcalfe et al., we find the $16 \text{ } \mu\text{m}$ counts down to $30 \text{ } \mu\text{Jy}$ appear to be resolving at least $\sim 50\%$ of the monochromatic $16 \text{ } \mu\text{m}$ EBL. Most likely the resolved fraction of the $15 \text{ } \mu\text{m}$ EBL is even larger since the IGL at the faintest flux limits probed by the *Spitzer* surveys (Figure 15) appears to be asymptoting towards a value of $\sim 3 \text{ nW m}^{-2}$ if extrapolated to zero flux.

In principle, the 16 and $24 \text{ } \mu\text{m}$ IGL should be similar as they are sampling mostly similar populations. Though, the $24 \text{ } \mu\text{m}$ band is more sensitive to higher redshifts and, as we have shown, the $16 \text{ } \mu\text{m}$ band picks up a slightly higher fraction of AGN. Our value is lower than the quoted estimate of the $24 \text{ } \mu\text{m}$ IGL obtained by Papovich et al. (2004) of $2.7_{-0.7}^{+1.1} \text{ nW m}^{-2} \text{ sr}^{-1}$. However, that result was obtained by measuring the $24 \text{ } \mu\text{m}$ number counts down to $60 \text{ } \mu\text{Jy}$ and extrapolating to fainter fluxes using a fit to the faint-end slope. If we extrapolate the $16 \text{ } \mu\text{m}$ source counts to fluxes 10 times fainter (down to $3 \text{ } \mu\text{Jy}$), assuming faint-end slope $\alpha = -1.9$, we obtain $IGL_{16} \sim 2.9 \text{ nW m}^{-2} \text{ sr}^{-1}$, in good agreement with the MIPS value.

Fadda et al. (2002) find that AGN contribute $\sim 17\%$ of the $15 \text{ } \mu\text{m}$ background (see also La Franca et al. 2007). Similarly, Matute et al. (2006) place a lower limit of the AGN contribution to the $15 \text{ } \mu\text{m}$ IGL of 4–10%, using only optically-selected AGN. We measure the IGL for the AGN among the $16 \text{ } \mu\text{m}$ GOODS sources, and find a contribution to the $16 \text{ } \mu\text{m}$ IGL of $\sim 15\%$ from X-ray and power-law selected AGN.

Spitzer measurements at 8 and 24 μm have typically determined a marginally smaller contribution to the IGL from AGN. Ballantyne & Papovich (2007) and Barmby et al. (2006) find contribution of $\sim 10\%$ to the 24 μm background based on X-ray selection of AGN. Most of these surveys also rely on X-ray selection of AGN, and Barmby et al. (2006) suggest that the AGN contribution be corrected upwards by a factor of 1.5 to account for Compton-thick sources. Brand et al. (2006) suggest that only 3–7% of the 24 μm background results from AGN, and Franceschini et al. (2005) place the contribution at 10–15% based on optical selection. Silva et al. (2004) note that the fractional AGN contribution is, itself, an upper limit to the contribution to the IGL from AGN radiation because significant IR light from these sources arises from the host galaxy.

5. Summary

We have presented source catalogs for Spitzer 16 μm observations of the GOODS fields using the Peak-up Imaging capability. We surveyed the ACS area (150 sq. arcminutes) to depths of 40 and 65 μJy (50% completeness) in the Northern and Southern fields, respectively. In the ~ 10 sq. arcmin of the UDF, we reach 30 μJy . We detect 840 (N) and 476 (S) objects. These observations are the widest contiguous-area PUI taken during the Spitzer mission, and among the deepest. The catalog will be available through the NASA/IPAC Infrared Science Archive (IRSA⁹).

We validate the photometry by demonstrating that the Spitzer SEDs of stars in the fields are consistent with standard templates from Spitzer spectroscopy. We compare PUI photometry with observations within GOODS North by ISOCAM and find reasonable agreement after color correction, though the uncertainties are large. Comparison with AKARI shows marginally significant disagreement ($\sim 30\%$), with Spitzer fluxes being higher. We match PUI sources within 1 arcsecond with Spitzer, Chandra and HST detections. We also report spectroscopic redshifts from the literature where available. The distribution of redshifts is similar to that for 24 μm sources despite the shallower MIR depth, suggesting that redshifts so far available are mostly limited by optical faintness. We flag sources in the catalog that may have quality issues: possible source confusion, bad concentration index, lower than expected signal-to-noise ratio, low coverage.

Preliminary analysis of the survey find the following:

- Matching 16 μm sources with Chandra hard-band detections finds that $\sim 11\%$ of PUI

⁹<http://irsa.ipac.caltech.edu>

sources have X-ray counterparts. Combining these sources with power-law MIR selection for obscured AGN finds that about 15% of objects in the catalog are potentially AGN. The fraction of AGN increases with increasing $16\ \mu\text{m}$ flux density.

- The 16 to $24\ \mu\text{m}$ ratio shows significant variation with redshift. Most sources lie within the locus expected for starbursts, IR luminous galaxies, and AGN. A ratio > 1.4 appears likely to select predominantly sources at $1.1 < z < 1.6$, where the minimum between PAH emission peaks (as well as the $9.7\ \mu\text{m}$ silicate absorption) redshifts into the $24\ \mu\text{m}$ passband. About 5% of $16\ \mu\text{m}$ sources meet this color selection, though few are selected as AGN by X-ray emission or power-law SEDs and so any AGN contribution must be heavily obscured.
- Galaxy number counts show good agreement with previous surveys at similar wavelengths (from ISOCAM and AKARI). The large number of sources and the two fields provide improvements in both the Poissonian errors and the effects of cosmic variance. AGN make substantial contribution to the number counts at bright fluxes.
- We measure the integrated galaxy light at $16\ \mu\text{m}$, as a lower limit on the contribution to the monochromatic IR background, to be $2.2 \pm 0.2\ \text{nW m}^{-2} \text{sr}^{-1}$. Extrapolating to fluxes 10 times fainter than the survey limit raises this value to $2.9\ \text{nW m}^{-2} \text{sr}^{-1}$, or 75% of the extragalactic background light. The contribution of sources which host AGN to the $16\ \mu\text{m}$ EBL is $\sim 15\%$, similar to the fraction found in $24\ \mu\text{m}$ surveys.

Future $15\ \mu\text{m}$ results are expected from AKARI. Significantly more area has been covered, which will allow improved study of rare sources. The Spitzer archive also contains many shallow (though small) fields which were obtained in parallel to spectroscopic observations (Fajardo-Acosta et al. 2010, in prep.). Confusion-limited $16\ \mu\text{m}$ observations were obtained by Spitzer in a small number of fields (e.g. Program ID=499; PI=Colbert). Finally, the recently launched WISE mission will include $12\ \mu\text{m}$ images over the whole sky

This work is based in part on observations made with the *Spitzer Space Telescope*, which is operated by the Jet Propulsion Laboratory, California Institute of Technology under NASA contract 1407. Support for this work was provided by NASA through an award issued by JPL/Caltech. This research has made use of the NASA/ IPAC Infrared Science Archive (IRSA), which is operated by the Jet Propulsion Laboratory, California Institute of Technology, under contract with the National Aeronautics and Space Administration.

REFERENCES

- Aharonian, F., et al. 2002, *A&A*, 384, L23
- Alexander, D. M., et al. 2003, *AJ*, 126, 539
- Altieri, B., et al. 1999, *A&A*, 343, L65
- Armus, L., et al. 2004, *ApJS*, 154, 178
- Armus, L., et al. 2007, *ApJ*, 656, 148
- Aussel, H., Cesarsky, C. J., Elbaz, D., & Starck, J. L. 1999, *A&A*, 342, 313
- Balestra, I., et al. 2010, *A&A*, 512, A12
- Ballantyne, D. R., & Papovich, C. 2007, *ApJ*, 660, 988
- Barger, A. J., Cowie, L. L., & Wang, W.-H. 2008, *ApJ*, 689, 687
- Barmby, P., et al. 2006, *ApJ*, 642, 126
- Beckwith, S. V. W., et al. 2006, *AJ*, 132, 1729
- Bertin, E., & Arnouts, S. 1996, *A&AS*, 117, 393
- Brand, K., et al. 2006, *ApJ*, 644, 143
- Brandl, B. R., et al. 2006, *ApJ*, 653, 1129
- Brandt, W. N., et al. 2001, *AJ*, 122, 2810
- Burgarella, D., Buat, V., Takeuchi, T. T., Wada, T., & Pearson, C. 2009, *PASJ*, 61, 177
- Casertano, S., et al. 2000, *AJ*, 120, 2747
- Cesarsky, C. J., et al. 1996, *A&A*, 315, L32
- Chapman, S. C., Blain, A. W., Smail, I., & Ivison, R. J. 2005, *ApJ*, 622, 772
- Chary, R., & Elbaz, D. 2001, *ApJ*, 556, 562
- Chary, R., et al. 2004, *ApJS*, 154, 80
- Cohen, J. G., Hogg, D. W., Blandford, R., Cowie, L. L., Hu, E., Songaila, A., Shopbell, P., & Richberg, K. 2000, *ApJ*, 538, 29

- Cohen, J. G. 2001, *AJ*, 121, 2895
- Croom, S. M., Warren, S. J., & Glazebrook, K. 2001, *MNRAS*, 328, 150
- Daddi, E., et al. 2007, *ApJ*, 670, 173
- Daddi, E., Dannerbauer, H., Elbaz, D., Dickinson, M., Morrison, G., Stern, D., & Ravindranath, S. 2008, *ApJ*, 673, L21
- Dawson, S., Stern, D., Bunker, A. J., Spinrad, H., & Dey, A. 2001, *AJ*, 122, 598
- Dickinson, M., Giavalisco, M., & GOODS Team 2003, *The Mass of Galaxies at Low and High Redshift*, 324
- Dole, H., et al. 2006, *A&A*, 451, 417
- Doherty, M., Bunker, A. J., Ellis, R. S., & McCarthy, P. J. 2005, *MNRAS*, 361, 525
- Donley, J. L., Rieke, G. H., Pérez-González, P. G., Rigby, J. R., & Alonso-Herrero, A. 2007, *ApJ*, 660, 167
- Donley, J. L., Rieke, G. H., Pérez-González, P. G., & Barro, G. 2008, *ApJ*, 687, 111
- Elbaz, D., et al. 1999, *A&A*, 351, L37
- Elbaz, D., Cesarsky, C. J., Chanical, P., Aussel, H., Franceschini, A., Fadda, D., & Chary, R. R. 2002, *A&A*, 384, 848
- Fadda, D., Flores, H., Hasinger, G., Franceschini, A., Altieri, B., Cesarsky, C. J., Elbaz, D., & Ferrando, P. 2002, *A&A*, 383, 838
- Franceschini, A., et al. 2005, *AJ*, 129, 2074
- Frayser, D. T., et al. 2006, *ApJ*, 647, L9
- Fruchter, A. S., & Hook, R. N. 2002, *PASP*, 114, 144
- Giacconi, R., et al. 2002, *ApJS*, 139, 369
- Giavalisco, M., et al. 2004, *ApJ*, 600, L93
- Gruppioni, C., Lari, C., Pozzi, F., Zamorani, G., Franceschini, A., Oliver, S., Rowan-Robinson, M., & Serjeant, S. 2002, *MNRAS*, 335, 831
- Hao, L., et al. 2005, *ApJ*, 625, L75

- Hauser, M. G., & Dwek, E. 2001, *ARA&A*, 39, 249
- Hopwood, R., et al. 2010, *ApJ*, 716, L45
- Houck, J. R., et al. 2004, *ApJS*, 154, 18
- Kasliwal, M. M., Charmandaris, V., Weedman, D., Houck, J. R., Le Floch, E., Higdon, S. J. U., Armus, L., & Teplitz, H. I. 2005, *ApJ*, 634, L1
- Kennicutt, R. C., Jr. 1998, *ARA&A*, 36, 189
- Kessler, M. F., et al. 1996, *A&A*, 315, L27
- Kriek, M., et al. 2008, *ApJ*, 677, 219
- Kurucz, R. L. 1979, *ApJS*, 40, 1
- Lagache, G., Puget, J.-L., & Dole, H. 2005, *ARA&A*, 43, 727
- Lacy, M., et al. 2004, *ApJS*, 154, 166
- La Franca, F., et al. 2007, *A&A*, 472, 797
- Laurent, O., Mirabel, I. F., Charmandaris, V., Gallais, P., Madden, S. C., Sauvage, M., Vigroux, L., & Cesarsky, C. 2000, *A&A*, 359, 887
- Le Borgne, D., Elbaz, D., Ocvirk, P., & Pichon, C. 2009, *arXiv:0901.3783*
- Le Fèvre, O., et al. 2004, *A&A*, 428, 1043
- LeFloch, E., et al. 2009, *ApJ*, 703, 222
- Luo, B., et al. 2008, *ApJS*, 179, 19
- Makovoz, D., & Marleau, F. R. 2005, *PASP*, 117, 1113
- Makovoz, D., Khan, I., & Masci, F. 2006a, *Proc. SPIE*, 6065, 330
- Makovoz, D., Roby, T., Khan, I., & Booth, H. 2006b, *Proc. SPIE*, 6274,
- Marleau, F. R., et al. 2004, *ApJS*, 154, 66
- Matsuura, S., et al. 2010, *arXiv:1002.3674*
- Matute, I., La Franca, F., Pozzi, F., Gruppioni, C., Lari, C., & Zamorani, G. 2006, *A&A*, 451, 443

- Metcalfe, L., et al. 2003, *A&A*, 407, 791
- Mignoli, M., et al. 2005, *A&A*, 437, 883
- Murakami, H., et al. 2007, *PASJ*, 59, 369
- Murphy, E. J., Chary, R.-R., Alexander, D. M., Dickinson, M., Magnelli, B., Morrison, G., Pope, A., & Teplitz, H. I. 2009, *ApJ*, 698, 1380
- Papovich, C., et al. 2004, *ApJS*, 154, 70
- Pearson, C. 2005, *MNRAS*, 358, 1417
- Pearson, C. P., et al. 2010, *A&A*, 514, A8
- Pope, A., et al. 2008, *ApJ*, 675, 1171
- Popesso, P., et al. 2009, *A&A*, 494, 443
- Puget, J. L., & Leger, A. 1989, *ARA&A*, 27, 161
- Ravikumar, C. D., et al. 2007, *A&A*, 465, 1099
- Reddy, N. A., Steidel, C. C., Erb, D. K., Shapley, A. E., & Pettini, M. 2006, *ApJ*, 653, 1004
- Renault, C., Barrau, A., Lagache, G., & Puget, J.-L. 2001, *A&A*, 371, 771
- Rieke, G. H., et al. 2004, *ApJS*, 154, 25
- Rodighiero, G., Lari, C., Fadda, D., Franceschini, A., Elbaz, D., & Cesarsky, C. 2004, *A&A*, 427, 773
- Sajina, A., Lacy, M., & Scott, D. 2005, *ApJ*, 621, 256
- Silva, L., Maiolino, R., & Granato, G. L. 2004, *MNRAS*, 355, 973
- Smail, I., Hogg, D. W., Yan, L., & Cohen, J. G. 1995, *ApJ*, 449, L105
- Smith, J. D. T., et al. 2007, *ApJ*, 656, 770
- Spoon, H. W. W., et al. 2004, *ApJS*, 154, 184
- Stern, D., et al. 2005, *ApJ*, 631, 163
- Strolger, L.-G., et al. 2004, *ApJ*, 613, 200

- Swinbank, A. M., Smail, I., Chapman, S. C., Blain, A. W., Ivison, R. J., & Keel, W. C. 2004, *ApJ*, 617, 64
- Szokoly, G. P., et al. 2004, *ApJS*, 155, 271
- Takagi, T., & Pearson, C. P. 2005, *MNRAS*, 357, 165
- Takagi, T., et al. 2007, *PASJ*, 59, 557
- Teplitz, H. I., Charmandaris, V., Chary, R., Colbert, J. W., Armus, L., & Weedman, D. 2005, *ApJ*, 634, 128
- Treister, E., et al. 2006, *ApJ*, 640, 603
- Treu, T., et al. 2005, *ApJ*, 633, 174
- Vanzella, E., et al. 2005, *A&A*, 434, 53
- Wada, T., et al. 2007, *PASJ*, 59, 515
- Weedman, D. W., et al. 2005, *ApJ*, 633, 706
- Werner, M. W., et al. 2004, *ApJS*, 154, 1
- Williams, R. E., et al. 1996, *AJ*, 112, 1335
- Wirth, G. D., et al. 2004, *AJ*, 127, 3121

Table 1. GOODS-N, Spitzer data

ID	RA	DEC	Cov ^a	f_{ch1}	σ_{ch1}	f_{ch2}	σ_{ch2}	f_{ch3}	σ_{ch3}	f_{ch4}	σ_{ch4}	f_{16}	σ_{16}	f_{24}	σ_{24}
(1)	(deg)	(deg)	(4)	(μ Jy)	(μ Jy)	(μ Jy)	(μ Jy)	(μ Jy)	(μ Jy)	(μ Jy)	(μ Jy)	(μ Jy)	(μ Jy)	(μ Jy)	(μ Jy)
0	189.319641	62.390766	11	84.80	4.24	60.40	3.02	55.20	2.94	40.20	2.16	145.1	11.3	225.0	5.5
1	189.310349	62.388977	12	11.50	0.58	14.50	0.73	19.00	1.50	12.90	0.99	55.3	10.4	200.0	5.7
2	189.326126	62.383057	20	38.30	1.92	49.10	2.46	55.30	2.83	39.30	2.06	107.2	16.5	483.0	5.7
3	189.294266	62.376274	20	40.00	2.00	47.50	2.38	39.60	2.11	44.20	2.30	240.4	11.5	386.0	4.9
4	189.330811	62.375191	24	10.10	0.51	6.98	0.36	7.48	0.63	6.27	0.63	53.9	11.5	26.6	5.6
5	189.284683	62.377537	15	33.50	1.68	30.20	1.51	21.00	1.40	20.50	1.24	96.0	18.3	89.1	6.2
6	189.301178	62.375061	21	10.90	0.55	10.50	0.53	8.67	0.75	11.60	0.82	75.5	11.7	60.5	3.6
7	189.317520	62.370590	27	28.40	1.42	24.10	1.21	20.70	1.15	34.00	1.78	129.3	14.6	133.0	4.9
8	189.314499	62.371925	26	1.16	0.08	1.13	0.10	0.47	0.52	3.13	0.56	56.7	11.3	50.7	4.0
9	189.306412	62.371181	22	50.70	2.54	37.50	1.88	32.20	1.70	30.10	1.60	339.4	13.7	436.0	5.8
10	189.266174	62.368641	19	7.67	0.39	5.57	0.30	4.81	0.84	4.93	0.72	62.8	15.0	18.3	4.6
11	189.292343	62.368526	18	32.10	1.61	29.90	1.50	21.80	1.23	23.50	1.30	130.8	12.8	125.0	4.0
12	189.351440	62.366024	21	242.00	12.10	199.00	9.95	131.00	6.57	214.00	10.71	365.8	17.6	395.0	7.7
13	189.351089	62.363888	21	18.80	0.94	14.00	0.70	12.40	0.77	14.00	0.87	62.8	11.8	60.5	6.2
14	189.281219	62.363293	15	47.40	2.37	51.00	2.55	52.10	2.66	59.60	3.03	129.2	16.5	240.0	3.4
15	189.276138	62.360157	22	101.00	5.05	103.00	5.15	117.00	5.88	123.00	6.17	219.1	14.1	303.0	5.2

^(a)Coverage in number of exposures (30 seconds integration per exposure).

Table 2. GOODS-N, ancillary data

z_{spec}	Ref. ¹	X ²	SB flux ³ (10^{-15}mW m^{-2})	HB flux ³	S ⁴	Ratio ⁵	N _{cl} ⁶	N _{cl16} ⁷	Q ⁸	E ⁹	B ¹⁰	V ¹⁰	I ¹⁰	z^{10} (mag)	σ_B^{10}	σ_V^{10}	σ_I^{10}	σ_z^{10}	Icls ¹¹
(17)	(18)	(19)	(20)	(21)	(22)	(23)	(24)	(25)	(26)	(27)	(28)	(29)	(30)	(31)	(32)	(33)	(34)	(35)	(36)
0.5820	72	0	0.000	0.000	0	2.32	1	1	1	0	-999.00	-999.00	-999.00	-999.00	-999.00	-999.00	-999.00	-999.00	0
-99.0000	-1	0	0.000	0.000	0	1.24	1	1	3	0	25.58	26.24	25.45	24.75	0.08	0.28	0.16	0.09	1
-99.0000	-1	0	0.000	0.000	0	3.09	1	1	1	0	26.85	26.14	25.80	25.01	1.45	0.19	0.17	0.09	1
1.5220	73	0	0.000	0.000	0	2.65	2	2	5	0	25.11	24.43	23.62	23.09	0.09	0.08	0.05	0.03	1
0.6760	72	0	0.000	0.000	0	1.76	1	1	9	0	24.71	23.68	22.82	22.59	0.04	0.03	0.02	0.01	1
-99.0000	-1	0	0.000	0.000	0	2.65	1	1	1	0	26.26	24.98	24.00	23.00	0.23	0.11	0.06	0.03	1
-99.0000	-1	0	0.000	0.000	0	2.04	1	1	1	0	27.90	27.02	25.50	24.44	0.50	0.34	0.11	0.05	1
0.5045	21	0	0.000	0.000	0	3.09	1	1	1	0	23.26	22.19	21.49	21.17	0.01	0.01	0.01	0.01	1
-99.0000	-1	0	0.000	0.000	0	3.72	1	1	1	0	25.82	25.51	25.04	24.54	0.08	0.06	0.05	0.04	1
0.9746	21	0	0.000	0.000	0	2.16	1	1	1	0	23.98	23.14	22.16	21.65	0.03	0.02	0.01	0.01	1
1.0084	21	0	0.000	0.000	0	3.61	1	1	9	0	24.38	23.96	23.27	22.90	0.02	0.02	0.01	0.01	1
1.3644	21	0	0.000	0.000	0	2.78	1	1	1	0	24.24	23.82	23.09	22.45	0.04	0.03	0.02	0.01	1
0.2810	21	0	0.000	0.000	0	3.27	1	2	5	0	20.70	19.13	18.39	18.07	0.01	0.01	0.01	0.01	1
0.8615	21	0	0.000	0.000	0	5.14	2	2	7	0	-999.00	-999.00	-999.00	-999.00	-999.00	-999.00	-999.00	-999.00	0
1.4498	21	1	8.270	14.120	0	2.14	1	1	1	0	22.97	22.77	22.37	21.98	0.01	0.01	0.01	0.01	1
0.9032	21	1	5.760	7.250	0	3.32	2	1	5	0	22.61	21.84	21.31	20.91	0.01	0.01	0.01	0.01	1

⁽¹⁾—1 no redshift; 10 – Cohen et al. (2000); Cohen (2001); 12 – Dawson et al. (2001); 21 – Wirth et al. (2004); 42 – Chapman et al. (2005), Swinbank et al. (2004); 45 – Pope et al. (2008), Murphy et al. (2009), Spitzer IRS redshifts; 51 – Treu et al. (2005); 61 – Reddy et al. (2006); 72 – Stern et al. (in prep.); 73 – Daddi et al. (2008); 81 – Barger et al. (2008)

²Xray detection (1=detected, 0=not detected)

³Alexander et al. (2003)

⁴Star flag (1=star, 0=galaxy)

⁵Concentration (ratio of apflux in 6:2 pixel radii)

⁶Number of ch4 sources within 4 arcsec radius

⁷Number of catalog sources within 5.4 arcsec radius

⁸Quality Flag is assigned Bitwise: Bit 0 = included in catalog; Bit 1 = more than one 16 micron source within 5.4 arcsec; possible confusion; Bit 2 = source concentration differs from that expected for point source; Bit 3 = S/N ratio < 5, but coverage indicates it should be higher

⁹Extend Flag (1=extended, 0=point source)

¹⁰Giavalisco et al. (2004)

¹¹Number of i-band sources within 1 arcsec radius

Table 3. GOODS-S, Spitzer data

ID	RA	DEC	Cov ^a	f_{ch1}	σ_{ch1}	f_{ch2}	σ_{ch2}	f_{ch3}	σ_{ch3}	f_{ch4}	σ_{ch4}	f_{16}	σ_{16}	f_{24}	σ_{24}
(1)	(deg)	(deg)	(4)	(μ Jy)	(μ Jy)	(μ Jy)	(μ Jy)	(μ Jy)	(μ Jy)	(μ Jy)	(μ Jy)	(μ Jy)	(μ Jy)	(μ Jy)	(μ Jy)
0	53.103943	-27.663679	2	29.60	1.48	20.80	1.05	23.70	1.37	17.00	1.10	120.5	23.7	120.0	5.7
1	53.142094	-27.664965	2	33.70	1.69	26.00	1.30	21.40	1.19	22.30	1.24	252.7	25.3	161.0	8.8
2	53.144711	-27.666069	3	171.00	8.55	149.00	7.45	112.00	5.62	576.00	28.81	830.6	39.8	938.0	11.5
3	53.110268	-27.667072	2	26.90	1.35	22.30	1.12	16.30	1.00	16.80	1.03	208.5	19.4	143.0	5.6
4	53.103607	-27.666225	4	21.10	1.06	19.70	0.99	13.80	0.92	13.00	0.90	81.8	14.6	44.2	4.9
5	53.102222	-27.669676	3	46.90	2.35	35.90	1.80	33.60	1.77	40.40	2.10	251.0	38.7	322.0	6.6
6	53.110622	-27.669182	3	31.10	1.56	26.90	1.35	20.50	1.17	17.30	1.04	99.2	17.9	74.0	5.4
7	53.123016	-27.669071	3	102.00	5.10	63.70	3.19	60.70	3.08	40.60	2.10	201.5	20.2	256.0	5.3
8	53.126549	-27.669138	3	25.90	1.30	26.20	1.31	19.70	1.11	19.90	1.14	174.7	15.9	118.0	5.1
9	53.129875	-27.671673	4	61.40	3.07	43.80	2.19	45.70	2.34	39.40	2.04	199.7	24.8	203.0	4.9
10	53.147671	-27.672302	4	44.70	2.24	39.10	1.96	27.80	1.47	25.60	1.38	158.2	24.8	108.0	4.9
11	53.102448	-27.672508	4	28.80	1.44	22.20	1.11	16.80	0.99	16.30	0.98	169.0	16.8	162.0	5.5
12	53.109512	-27.674276	4	28.50	1.43	22.10	1.11	19.20	1.08	22.10	1.23	180.3	17.4	175.0	11.9
13	53.114948	-27.674074	4	25.50	1.28	18.20	0.91	13.90	0.85	12.10	0.80	107.8	17.0	67.8	5.4
14	53.127071	-27.675257	4	33.80	1.69	32.10	1.61	25.40	1.35	19.10	1.09	116.0	16.5	57.1	3.9
15	53.090645	-27.675821	3	42.60	2.13	41.00	2.05	33.30	1.74	84.40	4.25	215.6	19.8	272.0	4.0

^(a)Coverage in number of exposures (60 seconds per exposure).

Table 4. GOODS-S, ancillary data

z_{spec}	Ref. ¹	X ²	SB flux ³ (10^{-15}mW m^{-2})	HB flux ³	S ⁴	Ratio ⁵	N _{cl} ⁶	N _{cl16} ⁷	Q ⁸	E ⁹	B ¹⁰	V ¹⁰	I ¹⁰	z^{10} (mag)	σ_B^{10}	σ_V^{10}	σ_I^{10}	σ_z^{10}	Icls ¹¹
(17)	(18)	(19)	(20)	(21)	(22)	(23)	(24)	(25)	(26)	(27)	(28)	(29)	(30)	(31)	(32)	(33)	(34)	(35)	(36)
0.6658	42	0	0.000	0.000	0	2.53	1	1	17	0	25.32	23.39	22.42	22.09	0.01	0.02	0.02	0.01	1
1.1120	30	0	0.000	0.000	0	3.31	2	1	27	0	23.07	22.54	21.96	21.52	0.01	0.01	0.01	0.01	1
0.2140	42	0	0.000	0.000	0	2.72	1	1	1	0	20.50	19.34	18.79	18.57	0.01	0.01	0.01	0.01	2
0.6243	1	0	0.000	0.000	0	2.49	1	1	17	0	26.43	24.76	23.77	23.06	0.01	0.05	0.04	0.02	1
-99.0000	-1	0	0.000	0.000	0	2.70	1	1	1	0	26.82	23.40	25.00	24.27	0.01	0.02	0.13	0.08	1
-99.0000	-1	1	0.000	1.300	0	2.58	2	1	3	0	24.53	23.66	22.55	21.91	0.04	0.02	0.01	0.01	1
-99.0000	-1	0	0.000	0.000	0	3.21	1	2	3	0	-999.00	27.25	27.28	25.01	-999.00	0.43	0.76	0.10	2
0.7343	42	0	0.000	0.000	0	2.30	1	1	1	0	23.46	22.25	21.08	20.64	0.03	0.01	0.01	0.01	1
1.3570	30	0	0.000	0.000	0	1.96	1	1	1	0	24.55	24.08	23.30	22.60	0.05	0.03	0.03	0.02	1
0.5659	42	0	0.000	0.000	0	2.53	1	1	1	0	22.93	21.69	20.86	20.52	0.02	0.01	0.01	0.01	1
1.1240	30	0	0.000	0.000	0	2.15	1	1	1	0	26.64	25.34	24.11	23.01	0.28	0.07	0.04	0.02	1
1.0368	42	0	0.000	0.000	0	2.88	1	1	1	0	25.21	24.09	23.14	22.48	0.09	0.02	0.02	0.01	1
1.0387	42	0	0.000	0.000	0	4.53	1	1	5	0	23.33	22.93	22.34	22.03	0.02	0.01	0.01	0.01	1
-99.0000	-1	0	0.000	0.000	0	2.15	1	1	1	0	23.68	23.23	22.46	21.92	0.04	0.02	0.02	0.01	1
-99.0000	-1	0	0.000	0.000	0	2.43	1	1	1	0	24.69	24.16	23.37	22.64	0.08	0.05	0.04	0.02	1
0.4260	72	0	0.000	0.000	0	2.85	1	1	1	0	22.06	20.98	20.47	20.20	0.01	0.01	0.01	0.01	1

¹1 = LeFevre et al. (2004) ; 2 – Szokoly et al. (2004) ; 3 – Croom et al. (2001) ; 9 – K20 Survey, Mignoli et al. (2005) ; 11 – Strolger et al. (2004) ; 30 – Vanzella et al. (2008) ; 41,42 – Popesso et al. (2009), Balestra et al. (2010) ; 62 – Doherty et al. (2005) ; 70 – Ravikumar et al. (2007) ; 72 – Stern et al. (in prep.) ; 81 – Kriek et al. (2008)

²Xray detection (1=detected, 0=not detected)

³Luo et al. (2003)

⁴Star flag (1=star, 0=galaxy)

⁵Concentration (ratio of apflux in 6:2 pixel radii)

⁶Number of ch4 sources within 4 arcsec radius

⁷Number of catalog sources within 5.4 arcsec radius

⁸Quality Flag is assigned Bitwise: Bit 0 = included in catalog; Bit 1 = more than one 16 micron source within 5.4 arcsec; possible confusion; Bit 2 = source concentration differs from that expected for point source; Bit 3 = S/N ratio < 5, but coverage indicates it should be higher; Bit 4 = source with coverage of two exposures instead of three

⁹Extend Flag (1=extended, 0=point source)

¹⁰Giavalisco et al. (2004)

¹¹Number of i-band sources within 1 arcsec radius

Table 5. Numbers of Sources

Field	Sources	Hard Xray	other power-law AGN	Blue ($f_{16}/f_{24} > 1.4$) ^a
North	840	96	9	55 (25)
South	476	58	14	51 (34)

^aThe number of sources with $f_{16}/f_{24} > 1.4$ and a 5σ detection at $24\ \mu\text{m}$, with either no spectroscopic redshift or a redshift $1.1 < z < 1.6$, indicating possible silicate absorption. The number in parenthesis indicates how many of these sources have a quality flag value of 1.

Table 6. Sensitivities

Quantity	North	South	UDF
Min Itime per pixel (s) ^a	300	120	600
Planned Itime per pixel (s)	600	120	960
Mode Itime per pixel (s)	630	270	2100
Min predicted depth ^b (μ Jy)	80	125	55
Mode predicted depth (μ Jy)	48	80	30
Mode measured Depth ^c (μ Jy)	45	80	30

^aMinimum exposure time per pixel for objects in the catalog

^bMinimum predicted 5σ depth using the exposure time calculator on the SSC website

^cMode of measured 5σ depth

Table 7. GOODS-North Galaxy Number Counts

S_{low} (mJy)	S_{high} (mJy)	S_{avg} (mJy)	$N_{galaxies}$	Observed dN/dS (deg ⁻² mJy ⁻¹)	Corrected dN/dS (deg ⁻² mJy ⁻¹)	Corrected $\delta dN/dS$ (deg ⁻² mJy ⁻¹)
0.025	0.040	0.034	13
0.040	0.056	0.048	106	3.0×10^5	4.5×10^5	1.6×10^4
0.080	0.112	0.096	151	1.1×10^5	1.3×10^5	9.6×10^3
0.112	0.159	0.136	128	6.6×10^4	7.1×10^4	6.0×10^3
0.159	0.224	0.192	93	3.4×10^4	3.4×10^4	3.5×10^3
0.224	0.317	0.271	61	1.6×10^4	1.6×10^4	2.0×10^3
0.317	0.448	0.382	45	8.2×10^3	8.2×10^3	1.4×10^3
0.448	0.632	0.540	22	2.8×10^3	2.8×10^3	7.4×10^2
0.632	0.893	0.763	11	1.0×10^3	1.0×10^3	4.0×10^2
0.893	1.262	1.078	3	1.9×10^2	1.9×10^2	1.6×10^2
1.262	1.783	1.522	2	9.1×10^1	9.1×10^1	7.3×10^1
1.783	2.518	2.150	0
2.518	3.557	3.037	0

Table 8. GOODS-South Galaxy Number Counts

S_{low} (mJy)	S_{high} (mJy)	S_{avg} (mJy)	$N_{galaxies}$	Observed dN/dS (deg ⁻² mJy ⁻¹)	Corrected dN/dS (deg ⁻² mJy ⁻¹)	Corrected δ dN/dS (deg ⁻² mJy ⁻¹)
0.025	0.040	0.034	14	3.1×10^5	6.2×10^5	1.4×10^5
0.040	0.056	0.048	20	2.6×10^5	3.7×10^5	8.4×10^4
0.056	0.080	0.068	38	1.5×10^5	1.8×10^5	2.8×10^4
0.080	0.112	0.096	107	9.2×10^4	1.2×10^5	1.0×10^4
0.112	0.159	0.136	109	5.9×10^4	6.6×10^4	6.0×10^3
0.159	0.224	0.192	83	3.2×10^4	3.4×10^4	3.6×10^3
0.224	0.317	0.271	45	1.2×10^4	1.2×10^4	2.1×10^3
0.317	0.448	0.382	21	4.0×10^3	4.0×10^3	1.1×10^3
0.448	0.632	0.540	11	1.5×10^3	1.5×10^3	6.0×10^2
0.632	0.893	0.763	10	9.6×10^2	9.6×10^2	4.1×10^2
0.893	1.262	1.078	3	2.0×10^2	2.0×10^2	1.6×10^2
1.262	1.783	1.522	1	4.8×10^1	4.8×10^1	3.9×10^1
1.783	2.518	2.150	2	6.8×10^1	6.8×10^1	5.5×10^1
2.518	3.557	3.037	1	2.4×10^1	2.4×10^1	1.9×10^1

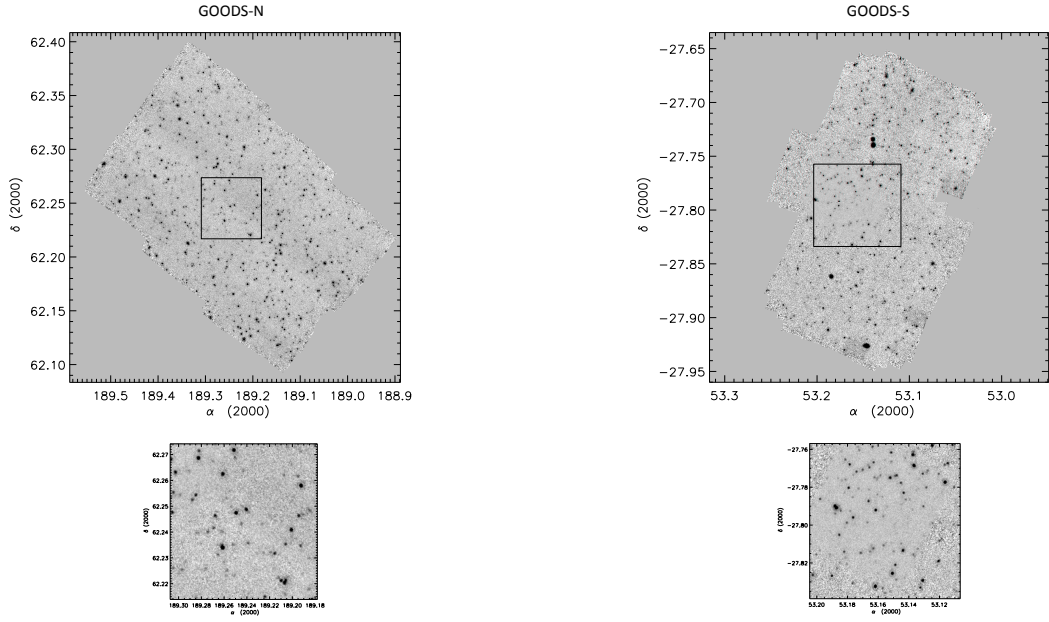


Fig. 1.— We show the mosaic of the North (left) and South (right) GOODS fields. A smaller region is shown below to give a better indication of crowding and image quality; for the South, the region includes the UDF, which has greater sensitivity than the rest of the field.

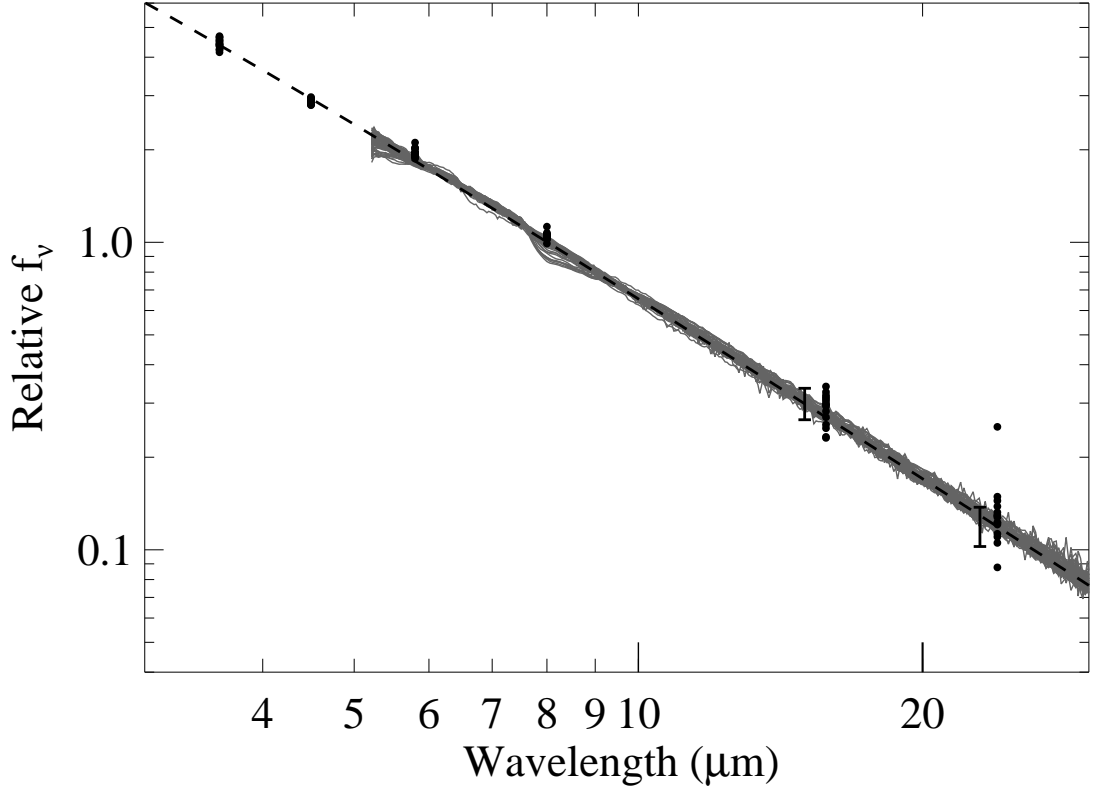


Fig. 2.— Spitzer photometry for 15 stars in GOODS (circles), normalized to the the average of the 6-band photometry. Data are compared to IRS spectra of stars with stellar types A through M (grey spectra) and the Kurucz (1979) model for an A0V star (dashed spectrum). The IRS spectra are taken from the SASS survey (Ardila et al. in prep). Error bars are small for the IRAC data points; typical error bars for the 16 and 24 μm photometry are shown next to the data.

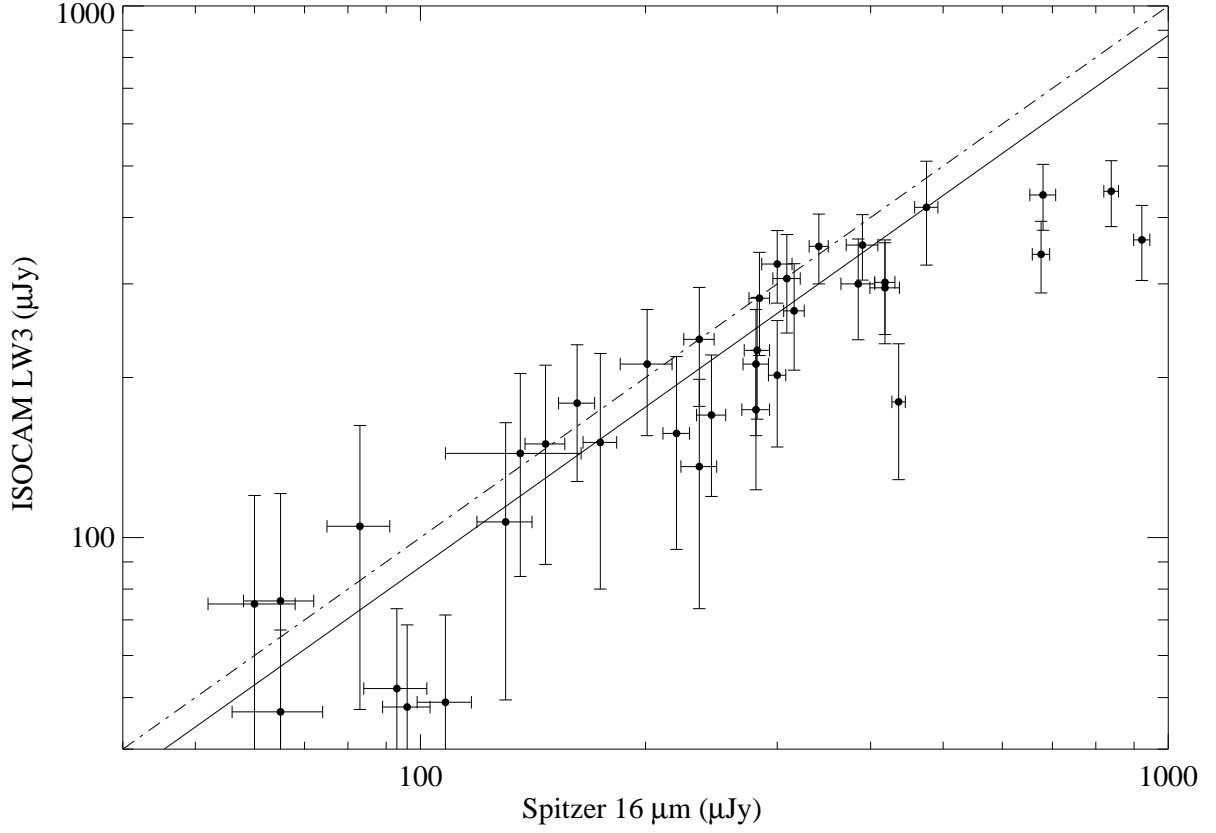


Fig. 3.— The flux density measured with *Spitzer* PUI in the $16\ \mu\text{m}$ bandpass compared to that measured with ISOCAM in the $15\ \mu\text{m}$ bandpass (LW3 Aussel et al. 1999, their Table 3) for objects detected by both instruments. The *dot-dashed* line indicates equal flux, and the *solid* line indicates the best fit offset of a factor of 1.13.

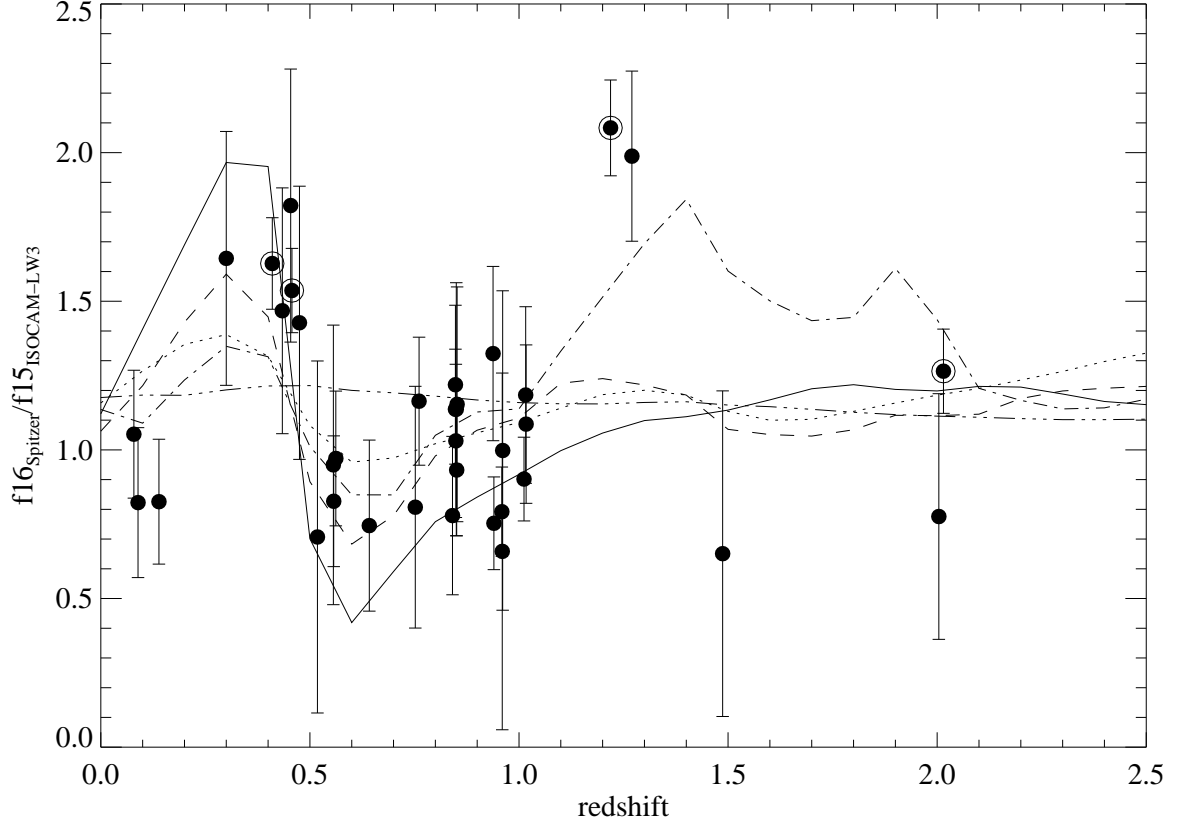


Fig. 4.— The ratio of the Spitzer 16 μm to ISOCAM 15 μm (LW3) flux densities as a function of spectroscopic redshift. The four brightest sources are circled. Also plotted are predicted ratios based on Spitzer IRS spectra of template galaxies: the extreme silicate-absorption galaxy IRAS F00183-7111 (Spoon et al. 2004, solid line), UGC5101, a ULIRG with considerable 9.7 μm absorption (Armus et al. 2004, dashed line), the prototypical AGN Mrk231 (Weedman et al. 2005, dotted line), the typical quasar PG1501+106 from (Hao et al. 2005, triple-dot-dashed line) and the average mid-IR SED of all starburst galaxies in the IRS GTO program from (Brandl et al. 2006, dot-dashed line).

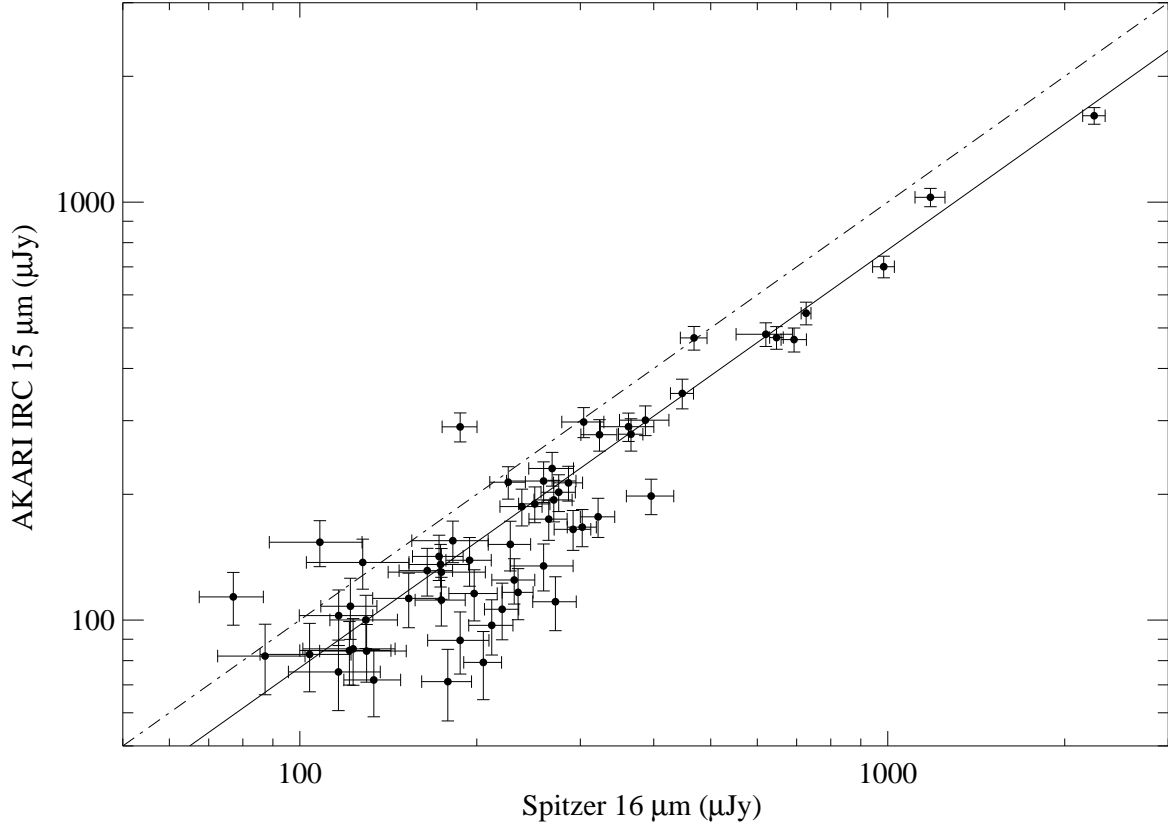


Fig. 5.— The flux density measured with *Spitzer* PUI in the 16 μ m bandpass compared to that measured with AKARI IRC in the 15 μ m bandpass (Burgarella et al. 2009) for objects detected by both instruments. The *dot-dashed* line indicates equal flux, and the *solid* line indicates the best-fit offset which corresponds to a factor of 1.3.

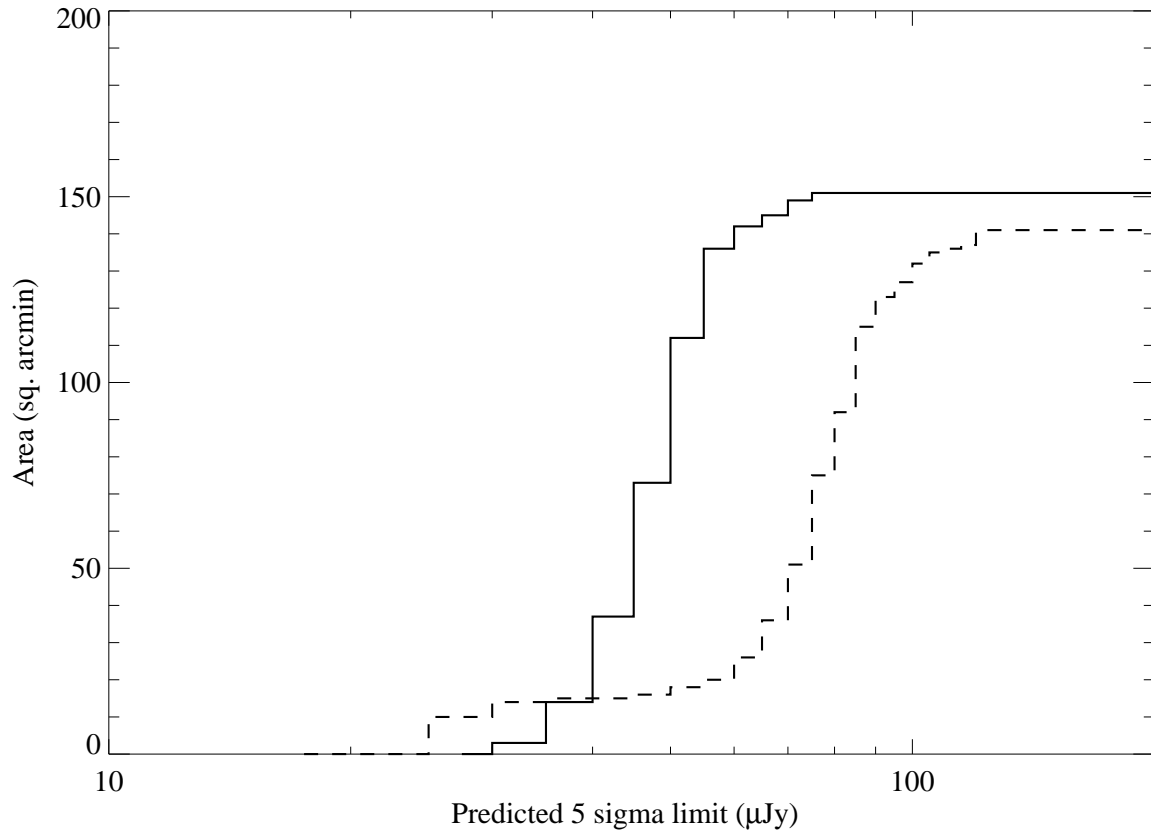


Fig. 6.— The area covered at expected sensitivity limits (in μJy) in the North (solid line) and South (dashed line). Sensitivity predictions are based upon the SSC exposure time calculator (see text).

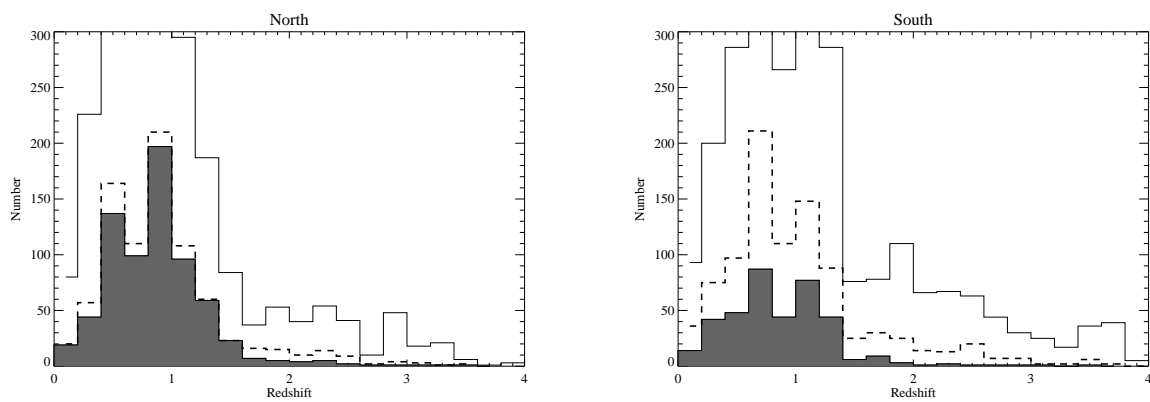


Fig. 7.— The distribution of spectroscopic redshifts (*filled histogram*) for sources associated with 16 μm detections in the North (*left*) and South (*right*), compared to the distribution of sources associated with 24 μm detections (*dashed line*) and the full spectroscopic sample (*solid line*; see text)

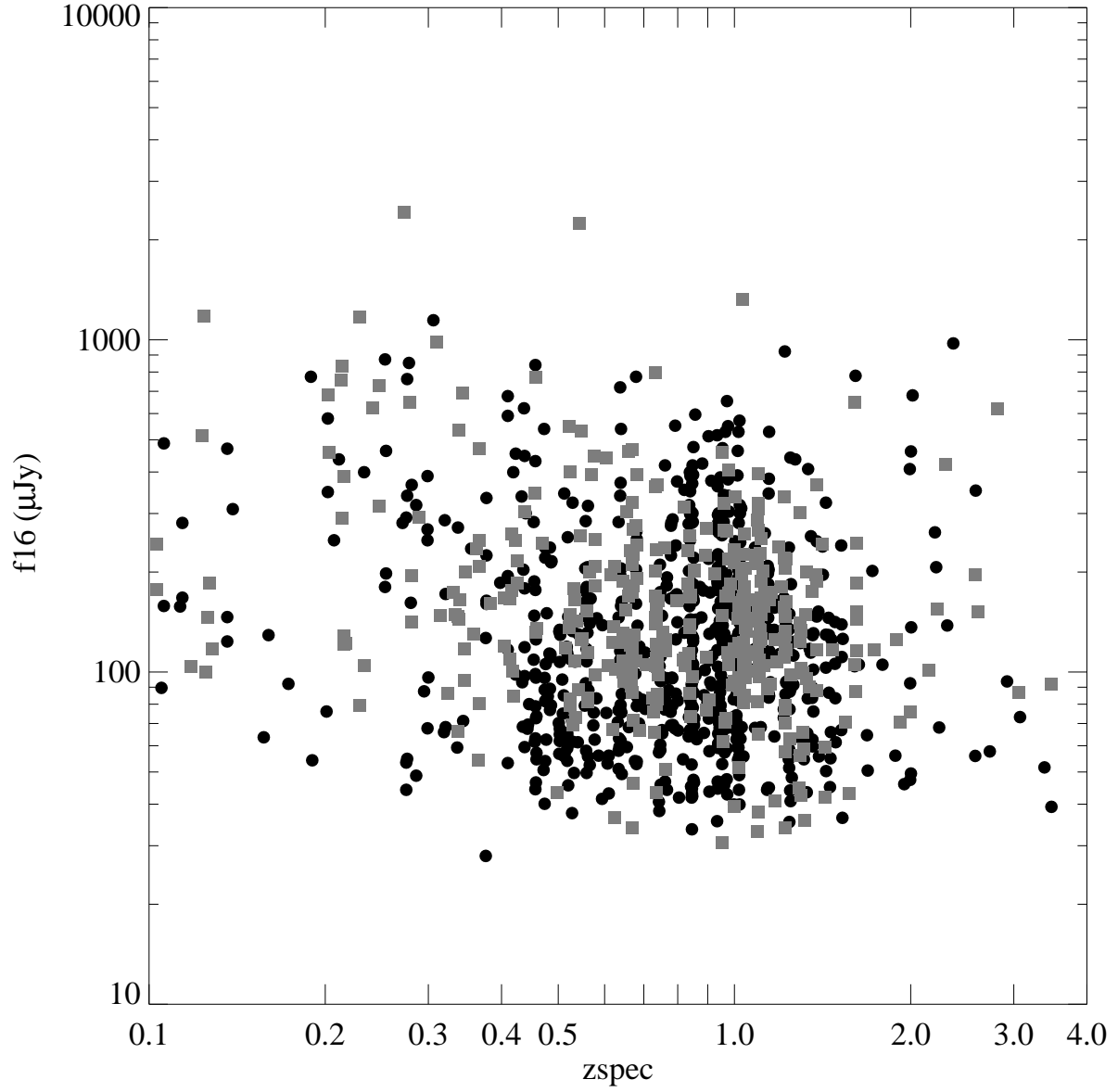


Fig. 8.— The flux density of 16 μm detected sources versus spectroscopic redshift for GOODS North (*black circles*) and South (*grey squares*).

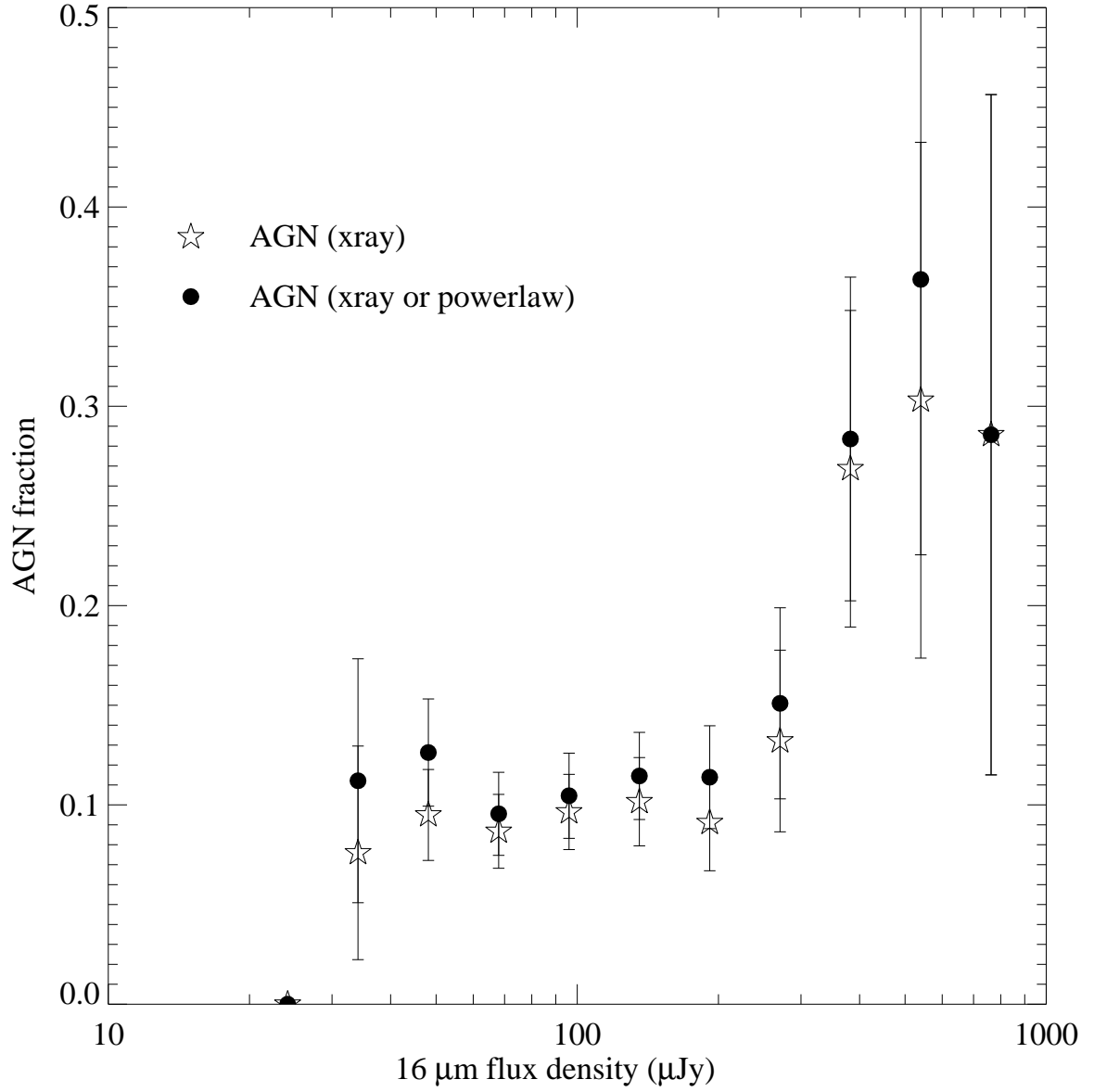


Fig. 9.— The fraction of 16 μm sources identified as AGN (*filled circles*) by the detection of hard X-rays (*open star symbols*) and/or power law slope.

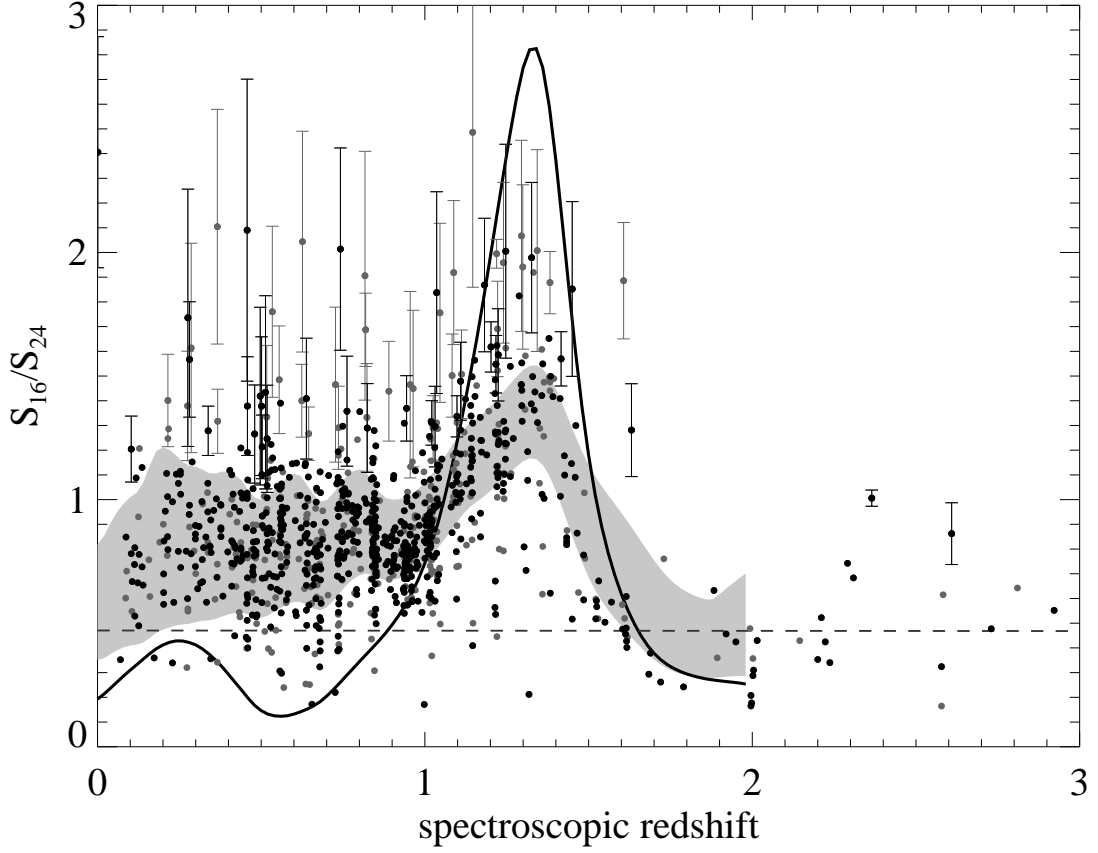


Fig. 10.— The ratio of 16 to 24 μm flux densities as a function of spectroscopic redshift for high quality (flag=1; *black points*) and all sources (*grey points*). The shaded region indicates the range of values expected from the starburst templates of Brandl et al. (2006) and Smith et al. (2007). The ratio for Arp220 (using the spectrum from Armus et al. 2007) is plotted (*solid line*), as is the value for a power law spectrum with $f_\nu \sim \nu^{-2}$ (*dashed line*). Uncertainties are plotted for objects with colors more than 1σ bluer than expected from the local starburst templates.

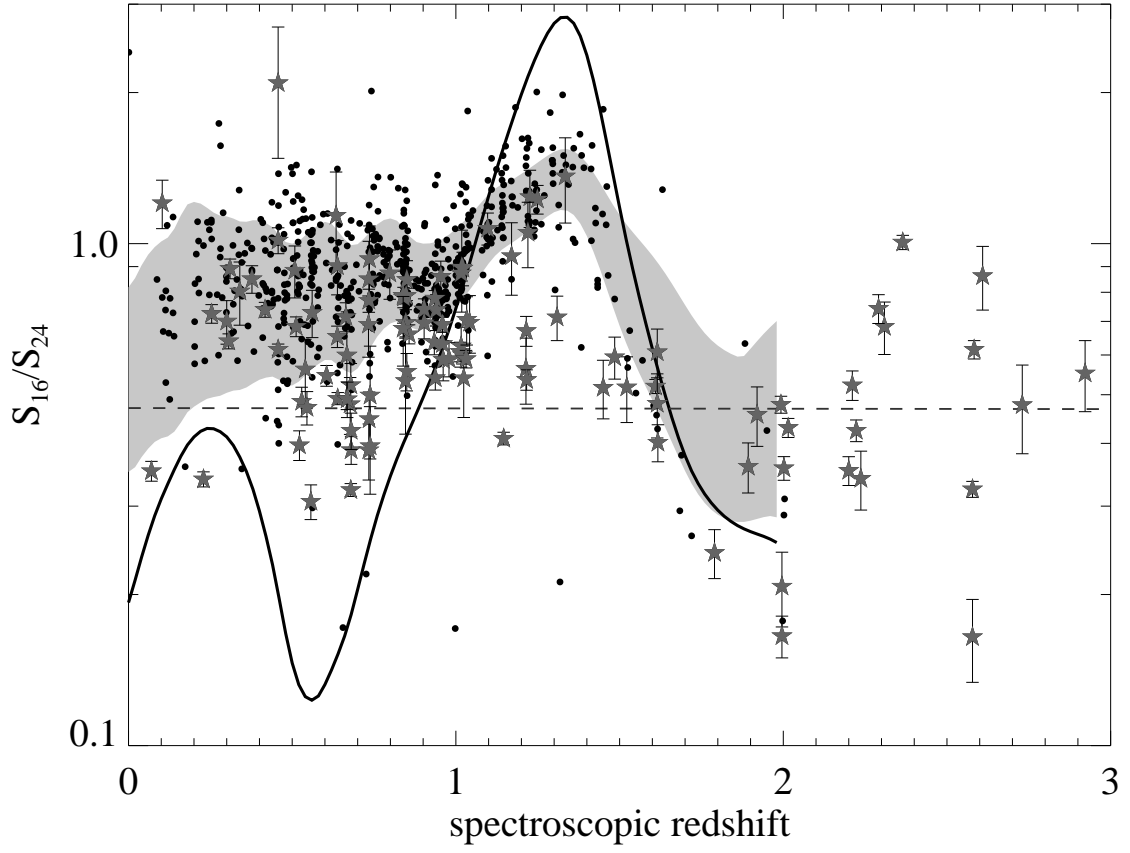


Fig. 11.— As in Figure 10, we show the flux ratio for high quality sources (flag=1; *black points*) and highlight objects identified as possible AGN through hard X-ray detection or power law slope (*star-shaped symbols*, see section 4.1).

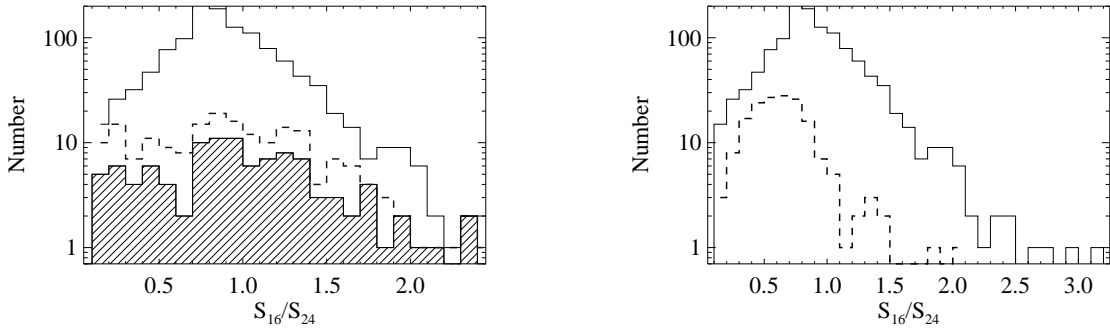


Fig. 12.— Histogram of 16 to 24 μm flux ratios for all objects (*solid line*) and objects without spectroscopic redshift (left; *filled histogram* for objects with photometry quality flag equal to 1; *dashed line* for all objects without redshift) and AGN (right; *dashed line*).

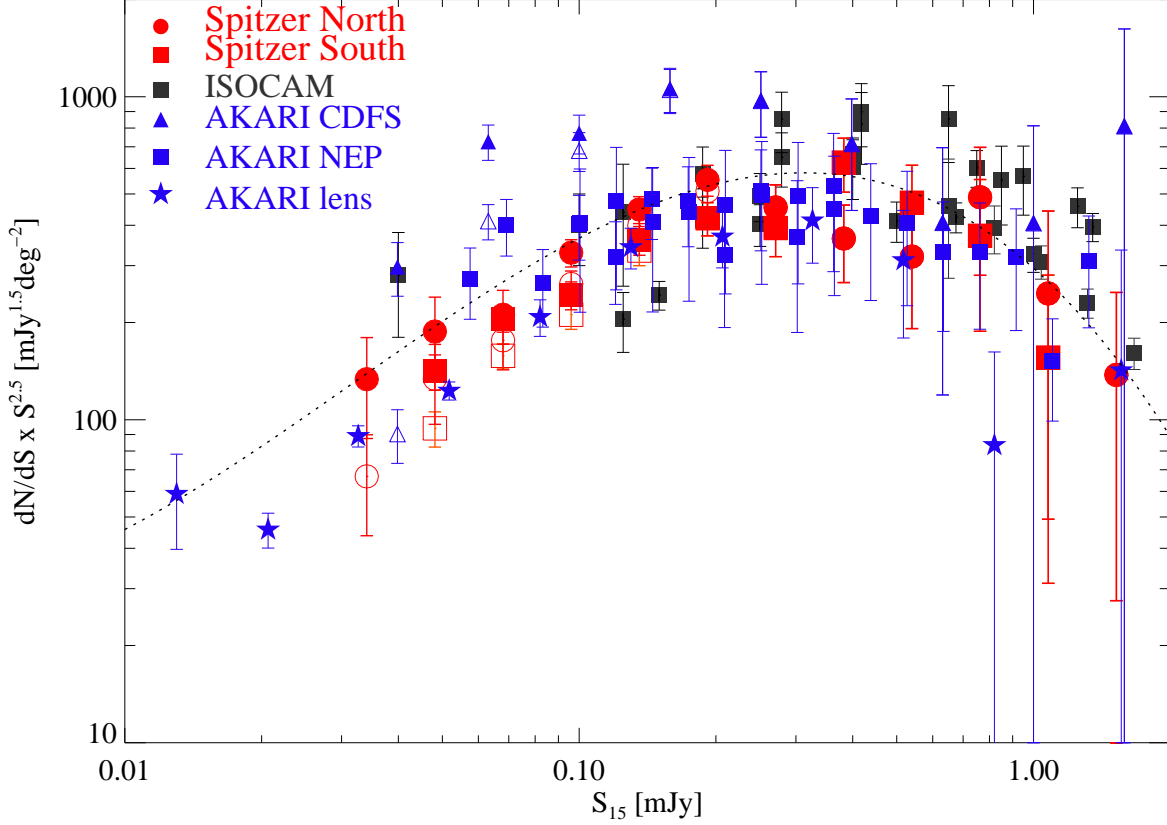


Fig. 13.— Differential 16 μm number counts measured by Spitzer (*filled red symbols* have completeness correction applied, *open red symbols* do not), AKARI (*blue symbols*), and ISO (*dark grey squares*). The Euclidean slope has been removed. Poissonian error bars are shown. ISOCAM points include HDF-N, HDF-S, and the Marano surveys (Elbaz et al. 1999, and the references therein); the gravitational lensing cluster survey (Altieri et al. 1999); the European Large-Area ISO Survey (ELIAS-S1; Gruppioni et al. 2002); and the Lockman Deep and Lockman Shallow surveys (Rodighiero et al. 2004). We plot AKARI points from the completeness-corrected counts measured in the North ecliptic pole (*filled squares*; Wada et al. 2007; Pearson et al. 2010). The Burgarella et al. (2009) survey of GOODS-South (*filled blue triangles* are counts with completeness correction, *open blue triangles* are the counts without) and we exclude bins with less than 20% completeness. We also show the completeness-corrected AKARI counts with lensed objects in Abell 2218 (Hopwood et al. 2010). We also show the fit to the combined Spitzer 16 μm counts from the two GOODS fields (*dotted line*; see Section 4.4)

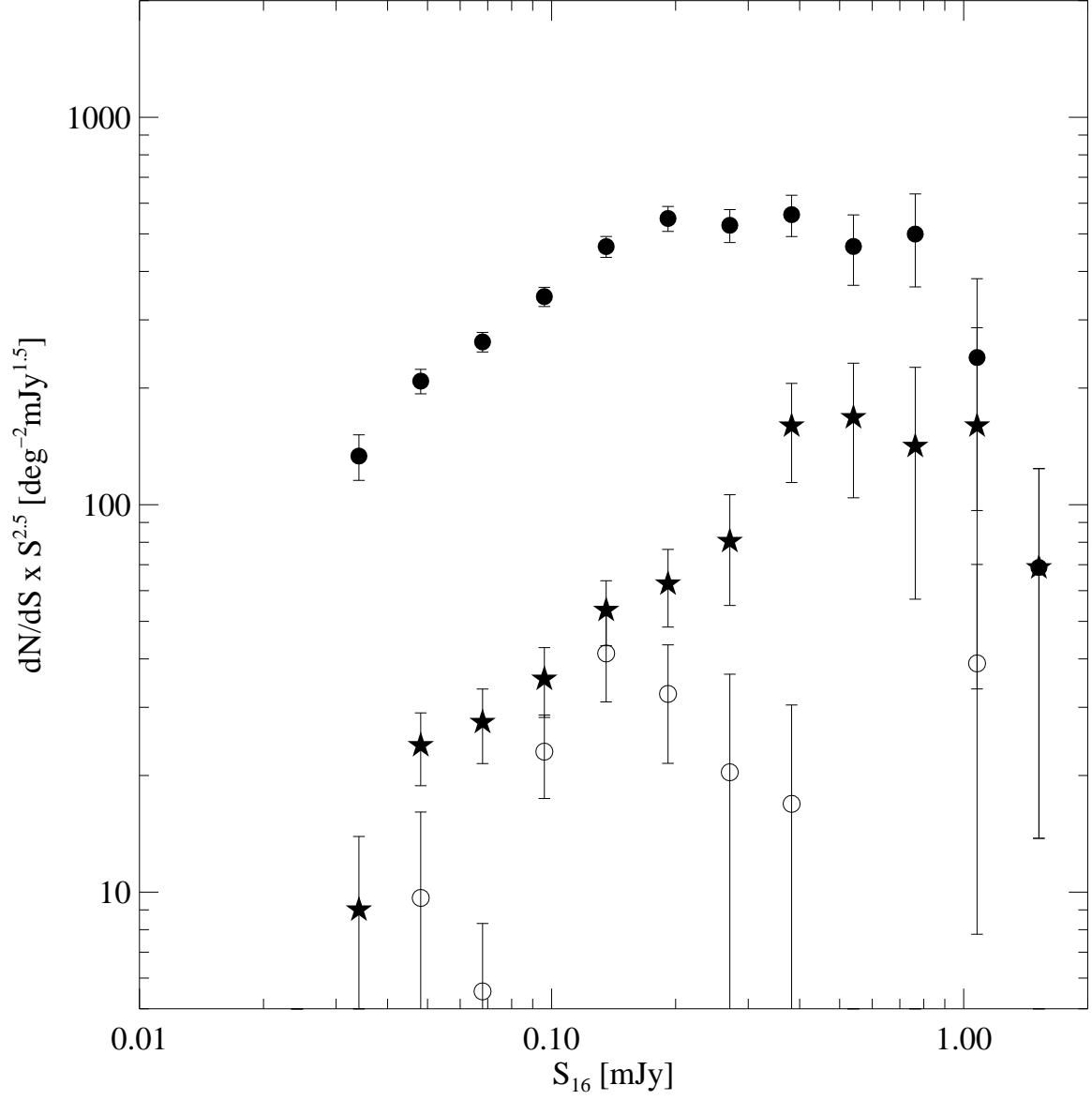


Fig. 14.— Differential 16 μ m number counts for GOODS North and South combined (*filled circles*). We show the contribution of sources identified as AGN (*star-shaped symbols*). We also show the contribution of objects with 16 to 24 μ m flux ratios > 1.4 , and spectroscopic redshifts $1 < z < 2$, indicating possible silicate absorption (*open circles*).

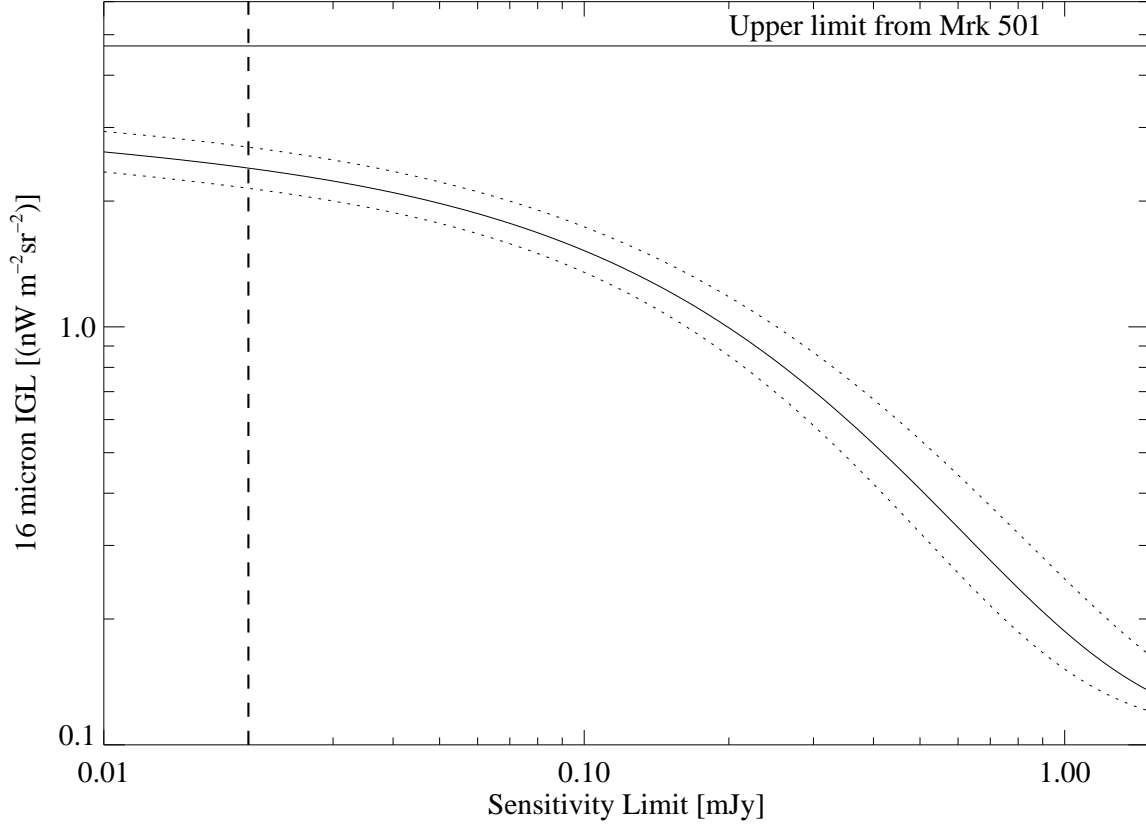


Fig. 15.— The integrated galaxy light (IGL) as a function of sensitivity limit. The IGL is extrapolated below the UDF sensitivity (*dotted vertical line*) assuming constant faint-end slope. The uncertainty (*dotted curve*) is estimated by calculating the IGL for the 1σ upper and lower limits to the number counts. The upper limit to the IGL is shown (Renault et al. 2001) as the *solid horizontal line*.